

On ocean and sea ice modes of variability in the Bering Sea

Seth Danielson,¹ Enrique Curchitser,² Kate Hedstrom,³ Thomas Weingartner,¹ and Phyllis Stabeno⁴

Received 17 June 2011; revised 17 October 2011; accepted 19 October 2011; published 23 December 2011.

[1] Results from a 35 year hindcast of northeast Pacific Ocean conditions are confronted with observational data collected over the Bering Sea shelf within the integration time period. Rotary power spectra of the hindcast currents near NOAA mooring site M2 site fall within the 95% confidence bounds for the observational spectra, except for a high bias in the counter-clockwise rotating component at 10 m depth in the high frequencies (periods <24 h). The model exhibits the most skill in reproducing anomalies of the integrated annual sea ice concentration and monthly subsurface (60 m depth) temperature fields, accounting for 85% and 50% of their observed variability. Analysis of the integrated ice concentration time series reveals evolution in the mean duration of ice-free waters (40 year trend of +6.8 days/decade) and changes in this parameter's variance with time. Correlation and empirical orthogonal function (EOF) analyses reveal the primary temporal-spatial patterns of variability in the temperature and salinity fields over the Bering Sea and northern Gulf of Alaska for near-surface (0–20 m) and subsurface (40–100 m) depth layers. Correlation analysis between the EOF principal components and various climate index and observed time series shows that the Pacific Decadal Oscillation, the North Pacific Gyre Oscillation, and the Bering Sea annually integrated ice area anomalies are important indices of thermohaline variability; the spatial structures of these modes give insight to their potential impacts upon the ecosystem. We identify a number of ecologically and economically important species whose temporal variability is significantly correlated with the identified spatial patterns.

Citation: Danielson, S., E. Curchitser, K. Hedstrom, T. Weingartner, and P. Stabeno (2011), On ocean and sea ice modes of variability in the Bering Sea, *J. Geophys. Res.*, 116, C12034, doi:10.1029/2011JC007389.

1. Introduction

[2] The physical oceanography of the eastern Bering Sea is influenced by tides, winds, buoyancy, topography, shelf-slope exchanges through canyons, flows through narrow passes and the yearly formation, drift, and melting of sea ice [Schumacher *et al.*, 2003]. The shelf supports a productive ecosystem, which delivers substantial benefit for both subsistence and commercial harvests, resulting in about half of the total U.S. fisheries landings [North Pacific Fishery Management Council (NPFMC), 2005]. There are also increasing levels of commercial vessel activity [Orr, 2011]. To better manage these interests, a fuller understanding of the Bering Sea's physical environment is required [Arctic Climate Impact Assessment (ACIA), 2005]. Our study provides a step toward this goal by the implementation, evaluation,

and analysis of a 35 year numerical hindcast of the thermohaline, circulation and ice fields with sufficient resolution to address some pertinent questions in the Bering Sea.

[3] The Bering Sea spans 20 degrees in longitude and 15 degrees in latitude (Figure 1). As a subarctic sea, seasonal variations in forcing are large and reflected in the circulation field, mixing and stratification, and sea ice distribution. Ecosystem structures are intrinsically tied to the physical features in the Bering Sea. For example, hydrographic features segregate predators from their prey (e.g., adult pollock from young of the year) [Wespestad *et al.*, 2000]; the strength of stratification impacts the success of euphausiids [Coyle *et al.*, 2008] and consequently the over-wintering success of juvenile pollock [Heintz and Vollenweider, 2010; Andrews *et al.*, 2011]; convergent fronts aggregate prey for feeding seabirds [Harrison *et al.*, 1990]. The location, timing, and thickness of sea ice cover impacts the trophic system: Pacific Walrus use the ice for resting and pupping [Fay, 1982], Spectacled Eiders use the St. Lawrence polynya as a winter feeding ground [Petersen *et al.*, 1999; Lovvorn *et al.*, 2003], late summer foraging by Thick-Billed Murres near the Pribilof Islands is observed to be related to the previous winter's ice extent [Kokubun *et al.*, 2010]. Hunt *et al.* [2002] propose that the timing of ice melt exerts a strong control on the timing of phytoplankton blooms and the fate (benthic/pelagic) of ice-edge production and zooplankton recruitment.

¹School of Fisheries and Ocean Science, Institute of Marine Science, University of Alaska Fairbanks, Fairbanks, Alaska, USA.

²Institute of Marine and Coastal Sciences, Rutgers, State University of New Jersey, New Brunswick, New Jersey, USA.

³Arctic Region Supercomputing Center, University of Alaska Fairbanks, Fairbanks, Alaska, USA.

⁴Pacific Marine Environmental Laboratory, NOAA, Seattle, Washington, USA.

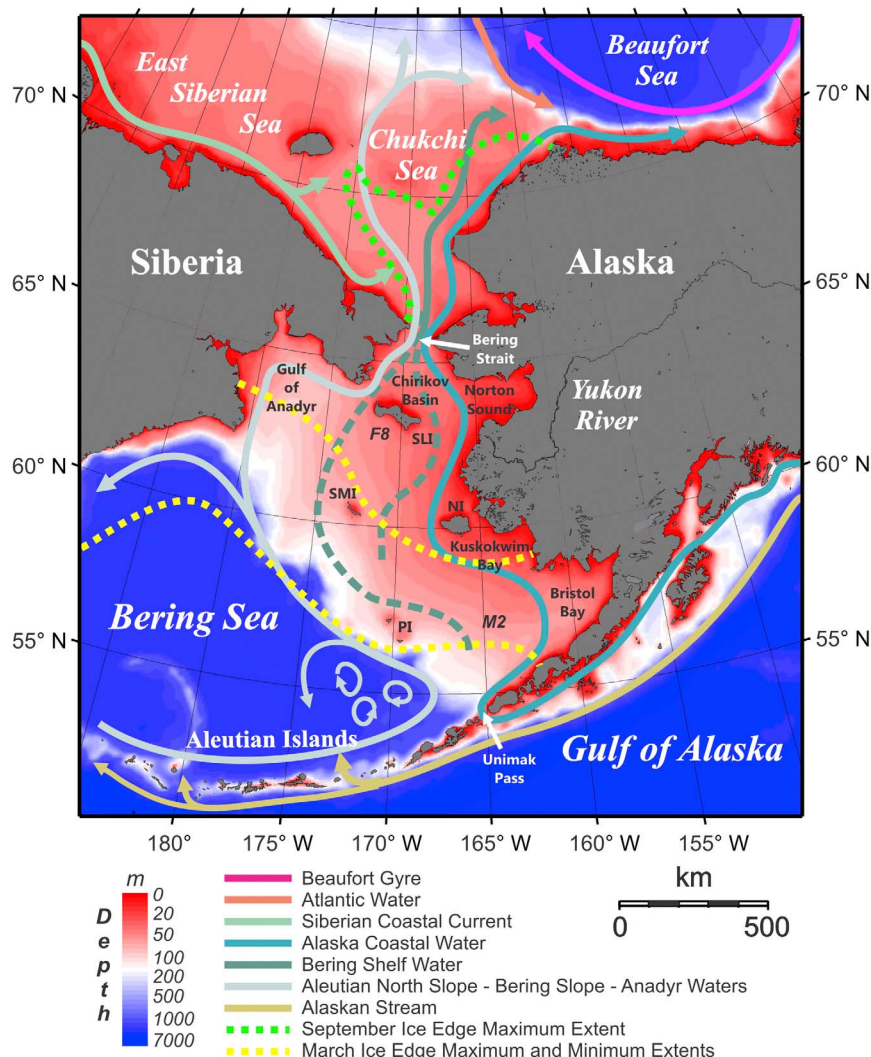


Figure 1. Schematic of the eastern Bering Sea and adjacent regions with major (idealized) summertime current and water mass features, typical spring and fall ice extent bounds, and place names. Mooring site and island abbreviations are as follows: F8, mooring F8; M2, mooring M2; SLI, St. Lawrence Island; NI, Nunivak Island; PI, Pribilof Islands; SMI, St. Matthew Island.

[4] Large interannual variability and multidecadal trends or regime shifts have been observed in many atmospheric and oceanographic parameters over the Bering Sea shelf [Overland *et al.*, 1999; Stephens *et al.*, 2001; Stabeno *et al.*, 2002b; Bograd *et al.*, 2005; Woodgate *et al.*, 2005; Rodionov *et al.*, 2007; Danielson *et al.*, 2011]. Many of these changes coincide with changes in the biota [Benson and Trites, 2002; Hunt *et al.*, 2002; Mueter and Litzow, 2008], including population changes in both managed and unmanaged species. Examples of such fluctuations include the onset of previously unobserved coccolithophorid blooms in the Bering Sea [Stockwell *et al.*, 2001], increases and subsequent decreases in the biomass of medusae [Brodeur *et al.*, 2002, 2008], variability in zooplankton biomass [Sugimoto and Tadokoro, 1997; Napp *et al.*, 2002], northward shifts of many groundfish species [Mueter and Litzow, 2008] and declines in bird and marine mammal populations [Byrd *et al.*, 1997; Trites *et al.*, 1999]. Many of the underlying causes of these population fluctuations are not known.

[5] The principal currents in the eastern Bering Sea basin are the Aleutian North Slope Current (ANSC) [Stabeno and Reed, 1994; Stabeno *et al.*, 1999], which flows eastward along the north side of the Aleutian Islands, and the Bering Slope Current (BSC) [Schumacher and Reed, 1992], which is fed by the ANSC and flows northward along the continental slope. Exchange between shelf and slope waters provides nutrients to maintain high production on the shelf [Coachman, 1986]. The controlling mechanisms are not well known although they are likely mediated by flow-topography interactions, slope current instabilities and tides [Schumacher and Reed, 1992; Stabeno and Van Meurs, 1999; Mizobata *et al.*, 2006]. Net flows over the eastern Bering Sea shelf are northward owing to a mean 0.8 Sv transport through Bering Strait [Roach *et al.*, 1995]. Wind-driven flows over the central shelf appear to laterally redistribute fresh water and heat on a seasonal basis [Danielson *et al.*, 2011]. On the inner Bering Sea shelf, the Alaska Coastal Current enters the Bering Sea through Unimak Pass from the Gulf of Alaska

(GOA). Shelf tides account for 50–95% of the total kinetic energy south of St. Lawrence Island [Coachman, 1986; Danielson and Kowalik, 2005]. The tides diffuse the ACC frontal system, which is fed in part by terrestrial runoff that occurs between Bristol Bay and Norton Sound [Coachman et al., 1975; Kachel et al., 2002].

[6] Vertical mixing due to tides, winds, and freezing compete with the stratifying tendencies of solar heating, river discharge, and ice melt. The resulting balance forms three distinct biophysical domains on the southeastern shelf [Coachman, 1982, 1986; Schumacher and Stabeno, 1998], which are nominally delineated by bathymetric strata. The coastal domain (0–50 m bottom depth) is well mixed or weakly stratified whereas the middle domain (50–100 m) consists of a strongly stratified two-layer system from spring through early fall. The outer domain (100 m to the shelfbreak) is more oceanic in character and includes surface and bottom mixed layers separated by a stratified layer.

[7] By the beginning of winter, ice forms over the northern shelf [Pease, 1980; Schumacher et al., 1982] and is advected as far south as the Alaska Peninsula in extreme years. The leading edge normally encounters melting throughout winter and ice retreat begins in the southeast Bering as early as February. However, ice can remain over the northern shelf well into June. These processes result in the annual formation of a “cold pool” (water <2°C) that forms over the northern shelf every year and over the southern shelf in years of extensive ice cover [Takenouti and Ohtani, 1974]. Fresh water from melting ice plays an important role in the spring setup of the stratified summer conditions on the northern shelf and much less so on the southern shelf [Stabeno et al., 2010]. The cold pool breaks down in the fall for a short period of time as wind mixing and surface heat losses drive water column homogenization.

[8] Our main objective is identifying dominant modes of interannual variability in the thermohaline and ice fields over the Bering Sea shelf on the basis of the results of a 35 year (1970–2005) integration of a three-dimensional coupled ocean-ice model. Before doing so, we quantitatively assess the skill of the model in order to show its value as a tool to study some aspects of this shelf and to identify some of the model’s limitations and capabilities. We compare model results to moored current/temperature/salinity records, satellite-derived sea ice concentrations, shipboard conductivity-temperature-depth (CTD) observations and tidal current/elevation harmonics. Temperature, salinity, and ice climatologies are removed in order to assess the model’s ability to hindcast observed anomalies with respect to the mean daily, monthly, or annual conditions.

[9] Previous numerical simulations of Bering Sea physical processes examine transport in straits and passes [Overland and Roach, 1987; Spaulding et al., 1987; Overland et al., 1994; Hu and Wang, 2010], sea ice dynamics [Kantha and Mellor, 1989; Pease and Overland, 1989; Pritchard et al., 1990; Zhang and Hibler, 1991; Clement et al., 2004], tides [Kowalik, 1999; Kowalik and Stabeno, 1999; Danielson and Kowalik, 2005; Foreman et al., 2006], storm surges [Johnson and Kowalik, 1986], and shelf circulation [Brasseur, 1991; Nihoul et al., 1993; Hermann et al., 2002]. Three-dimensional coupled ice-ocean models have been applied to the entire Bering Sea with the primary focus being on mass transports and sea ice dynamics [Clement et al., 2005;

Clement Kinney et al., 2009; Wang et al., 2009; Hu and Wang, 2010; Zhang et al., 2010].

[10] Our model falls into this latter category and we refer to it as the northeast Pacific model-5 (called NEP5 hereafter because the current implementation represents the fifth major code and grid iteration). It was initially developed as a component of the Northeast Pacific Global Ocean Ecosystem Dynamics (GLOBEC) program [Curchitser et al., 2005] and its results (from previous versions) were used directly or as boundary conditions for a variety of Bering Sea and Gulf of Alaska studies [Lankbury et al., 2007; Dobbins et al., 2009; Hermann et al., 2009a, 2009b; Fiechter et al., 2009; Hinckley et al., 2009]. Curchitser et al. [2010] ran the NEP5 model in a study supporting evaluation of potential impacts associated with possible offshore hydrocarbon development on the southeast Bering shelf. NEP5 results provide boundary conditions for multicomponent ecosystem models that are part of the North Pacific Research Board’s (NPRB) *Bering Ecosystem Study and Bering Sea Integrated Ecosystem Research Project (BEST-BSIERP)* [2010].

[11] The manuscript is organized as follows. The model formulation is described in section 2 and the observational data sets are described in section 3. Model-data comparisons are presented in section 4. The comparisons show that, in aggregate, the model integrations provide useful proxy time series that extend in situ ice, salinity, temperature and velocity observations over the integration period and domain. In section 5, we use trend, correlation and empirical orthogonal function (EOF) analyses to identify patterns of variability and their relation to fluctuations in ecosystem and climate records.

2. Numerical Model Description

[12] We implemented a coupled ocean/sea ice model based on the Regional Ocean Modeling System (ROMS), building upon Curchitser et al. [2005]. ROMS is a free-surface, hydrostatic primitive equation ocean circulation model (subversion accessed via Git at <https://www.myroms.org/> on 10 March 2010). It is a finite volume (Arakawa C-grid) model with several advanced features including sustained performance on multiprocessor computing platforms using Message Passing Interface (MPI) communication protocol; high-order, weakly dissipative algorithms for tracer advection; a unified treatment of surface and bottom boundary layers (e.g., K profile parameterization) [Large et al., 1994], and atmosphere-ocean flux computations based on the ocean model prognostic variables using bulk-formulae [Large and Yeager, 2009]. The vertical discretization is based on a terrain-following coordinate system with the ability to increase the resolution near the surface and bottom boundary layers.

[13] The foundation of the sea ice module is described by Roed and Debernard [2004] and was implemented in ROMS by Budgell [2005]. The algorithms consist of the elastic-viscous-plastic (EVP) rheology [Hunke and Dukowicz, 1997; Hunke 2001] and thermodynamics by Mellor and Kantha [1989]. It is fully explicit, implemented on the ROMS Arakawa C-grid, and therefore fully parallel using MPI. The model also includes frazil ice growth in the ocean being passed to the ice [Steele et al., 1989]. It currently follows a single ice category, which exhibits accurate results in a marginal ice zone such as the Bering Sea.

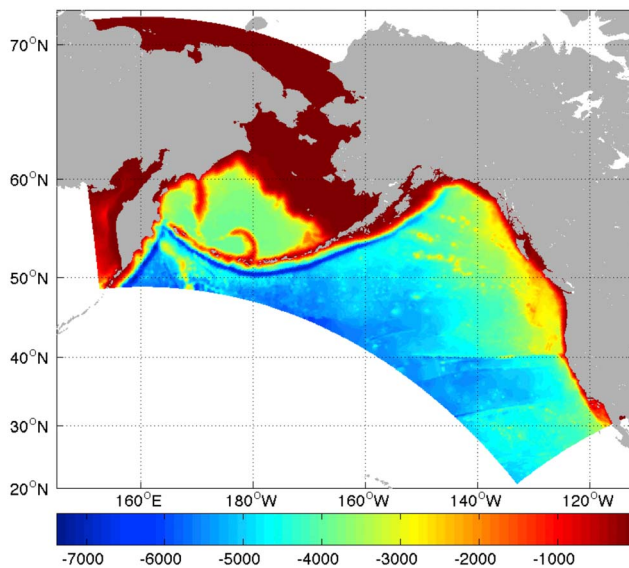


Figure 2. NEP5 model domain extent and bathymetric depths plotted on a Mercator projection map.

[14] One-way nesting was implemented using a hybrid of nudging and radiation approaches [Marchesiello *et al.*, 2001]. The global-to-regional downscaling via open boundary conditions has several desirable features for the implementation of regional models: for multidecadal integrations, climate signals project onto the high-resolution inner domains through boundary forcing; tidal forcing is naturally implemented on the domain's open boundaries but for extensive integrations a tidal potential correction is applied to ensure proper tidal phasing. The approach allows affordably generating ensembles of high-resolution, multidecadal simulations with realistic boundary forcing and provides the ability to test the robustness of solutions and understand model errors.

[15] The NEP5 model domain (Figure 2) extends from $\sim 20^\circ\text{N}$ to 71°N and extends 2250 km offshore from the North American coast at a nominal horizontal resolution of 10 km and with 60 vertical levels stretched toward the surface boundary. The grid (a rectangle in a Lambert Conical projection) is rotated relative to lines of constant longitude so as to minimize computations over land.

[16] We generated our own bathymetric grid by compiling an extensive collection of bottom soundings from sources that include the National Ocean Service hydrographic trackline database, soundings from NOAA's Electronic Navigational Charts (ENCs), other U.S. trackline/multibeam data archives and scientific research cruises. We also incorporated ENC soundings from the Canadian Hydrographic Service. In Russian waters, point soundings from nearly 150 historical Russian military nautical charts were digitized and georeferenced. The resulting compilation of sounding data was gridded to a regular 30 arc sec (~ 1 km) mesh with the Generic Mapping Tools [Wessel and Smith, 1991] suite of algorithms and the final gridded DEM is publicly available for download (www.ims.uaf.edu/~seth/bathy/). The Alaska region grid spans 130°E to 120°W and 45°N to 75°N . The final grid was smoothed, subsampled, and merged with the General Bathymetric Chart of the Oceans [British Oceanographic Data Centre, 2003] grid at 45°N in order to complete

the coverage across the southern portion of the domain. Maximum grid stiffness ratios $rx0 = 0.42$ [Haidvogel and Beckmann, 1999] and $rx1 = 24$ [Haney, 1991] imply that while the model likely has some difficulty in regions of steep topography such as near the Aleutian Islands, our focus area of the greater shelf should not be adversely impacted by baroclinic pressure gradient errors.

[17] We integrated the model from January 1969 to November 2005. Spin-up adjustments are evident in the 1969 thermohaline fields and so our analyses are based only on the 1970–2005 results. The surface forcing for the NEP model is derived from the Common Ocean-ice Reference Experiments (CORE) [Large and Yeager, 2009], which consists of 6 hourly winds, air temperatures, sea level pressure and specific humidity, daily short-wave and downwelling long-wave radiation, and monthly precipitation. The air-sea fluxes are computed using bulk formulae [Large and Yeager, 2009]. The oceanic surface boundary layer is computed using the k profile parameterization [Large *et al.*, 1994]. To ensure stability in regions with near-resonant tides (e.g., Bristol Bay and Cook Inlet), bottom stress is parameterized with a spatially variable linear coefficient of friction based on total water column depth, varying from $3 \times 10^{-4} \text{ m s}^{-1}$ for depths deeper than 1000 m to $6 \times 10^{-3} \text{ m s}^{-1}$ at 10 m depth. Surface salinities are restored to the monthly Polar Science Center Hydrographic Climatology (PHC), version 3.0, of Steele *et al.* [2001]. River discharge is implemented as a spatially dependent, time invariant surface fresh water flux, which is designed to preserve regional fresh water budgets. Boundary and initial conditions for this domain were derived from the Simple Ocean Data Assimilation (SODA) ocean reanalysis [Carton and Giese, 2008]. The geographical northern boundary has a sink term that enforces a constant 0.8 Sv northward transport through the Bering Strait.

3. Methods and Data

3.1. Model Output and Evaluation Metrics

[18] Model output files containing results from the entire computational grid are stored as daily and monthly averages; nearly 200 individual grid points (most located near historical mooring deployment sites) are also stored at hourly intervals at all depth levels. Numerous shorter integrations were performed in order to spot-check and tune model performance before the full 35 year integration was executed. All results presented in this manuscript are from NEP5 integration 42 except for the cotidal chart (Figure 3), which was generated by integration 45 and which output hourly records for the entire grid over a time period of 6 months.

[19] With the exception of the tidal harmonic parameters, which do not require coincident analysis, model results extracted for comparison conform to the same time window and latitude, longitude and depth of the observations. We avoid temporally discrete and singular model/data comparisons where possible, focusing instead on the bulk statistics of measurement ensembles. The exception to this is that in comparisons with CTD data: the model's daily mean T/S profile for the specific day sampled is employed at the grid point closest to the sampling location.

[20] We quantitatively compare the model with the observations following Willmott *et al.* [1985] and Taylor [2001] using the mean, standard deviation, cross correlation, and

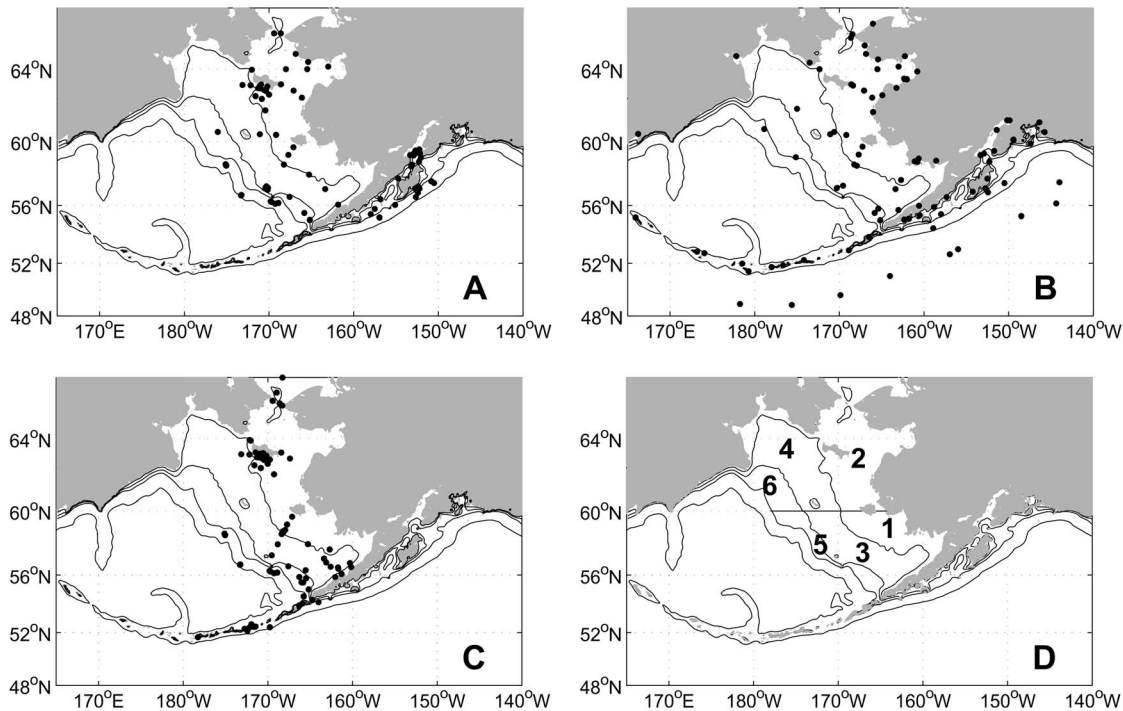


Figure 3. Locations of data employed in model evaluations: (a) moored current meter sites with tidal ellipse parameters, (b) moored and coastal sea level elevation stations with tidal amplitude parameters, (c) moored current meter sites with mean speed and direction statistics, and (d) regions 1–6 bound CTD and discrete bottle samples listed in Table 2. Contours are drawn at 50, 100, 200, and 2000 m depths.

root-mean-square difference (RMSD) as comparative metrics. Taylor diagrams [Taylor, 2001] facilitate incorporating all of these parameters into one graphic, which we use for the comparisons between the model and discrete CTD observations. Following Taylor [2001], the approach uses the pattern root-mean-square difference $RMSD' = \sqrt{\sigma_M^2 + \sigma_O^2 - \sigma_M \sigma_O r}$, where σ is the standard deviation, r the cross correlation and subscripts M and O refer to the model and observations, respectively. The prime indicates that values are normalized so that the observational data represent unity variance, unity autocorrelation and zero RMSD', allowing multiple comparisons to be shown on a single graphic. Rotary power spectra and least squares harmonic fits for tidal parameters are used in other comparisons.

3.2. Time Series Data for Model Evaluation

[21] We employ tidal amplitude and current harmonic parameters and net speed and direction statistics from various sources (Table 1) and locations (see Figures 3a–3c). Tidal parameters for measurements made by the National Data Buoy Center North Pacific Deep-Ocean Assessment and Reporting of Tsunamis DART moorings (www.ndbc.noaa.gov) were computed using the MATLAB based T_TIDE algorithms of Pawlowicz *et al.* [2002]. For the net speed and direction statistics (based on 177 observational records), the shortest averaging period is 1.6 months, the longest is 24 months, the mean length is 7.6 months, and the median record length is 5.1 months. Schumacher and Kinder [1983] provide the greatest number of net speed and direction records, but the deployment intervals are not explicitly tabulated so we estimated each record's start and stop date from

their (graphical) Table 1. We believe that the accuracy in selecting the record endpoints is good to within half a month. This uncertainty is associated with larger differences between the model and observed fields and degrades the accuracy of comparisons for the shorter records. Thus we neglect Schumacher and Kinder [1983] records that are <6 months.

[22] Temperature, salinity and current velocity time series records from the NOAA EcoFOCI program's mooring M2 (56.88°N, 164.06°W, 72 m water depth) between 1995 and 2005 are reanalyzed to compare the observed thermohaline annual cycle, monthly anomalies and current spectra with corresponding analyses from the model results.

3.3. CTD and Bottle Data

[23] CTD and discrete bottle data are from the National Ocean Data Center (NODC) World Ocean Database 2009 (WOD-09) [Boyer *et al.*, 2009], the U.S. Bering-Aleutian Salmon International Survey (BASIS) program, the Bering Ecosystem Study (BEST) and miscellaneous cruises from the UAF Institute of Marine Science's (IMS) database, which includes cruise data from the 1970s to the present. We limit analysis to one near-surface depth level (10 m depth) and one depth level below the summer pycnocline (70 m depth). Multiple observations recorded within the same model grid cell and sampled on the same year-month-day were averaged, resulting in 5939 unique observations at 70 m depth and 11,500 at 10 m depth. Data were grouped into regions that coarsely represent six major biophysical domains over the eastern shelf (see Figure 3d and Table 2). Regions 1, 3 and 5 represent the inner, middle and outer shelf domains south of

Table 1. Sources of Historical Tidal Parameters, Moored Time Series Data, and Net Speed and Direction Statistics Used in Model Evaluations^a

Source	Parameters or Data Set
<i>Muench and Schumacher</i> [1980]	tidal harmonics
<i>Pearson et al.</i> [1981]	tidal harmonics
<i>Schumacher et al.</i> [1982]	net speed/direction
<i>Schumacher and Kinder</i> [1983]	net speed/direction
<i>Schumacher et al.</i> [1983]	net speed/direction
<i>Mofjeld</i> [1984]	tidal harmonics
<i>Mofjeld et al.</i> [1984]	tidal harmonics
<i>Mofjeld</i> [1986]	tidal harmonics
<i>Greisman</i> [1985]	tidal harmonics
<i>Isaji and Spaulding</i> [1987]	tidal harmonics
<i>Muench et al.</i> [1988]	net speed/direction
<i>Schumacher and Reed</i> [1992]	tidal harmonics and net speed/direction
<i>Roach et al.</i> [1995]	net speed/direction
<i>Kowalik and Stabeno</i> [1999]	tidal harmonics
<i>Stabeno et al.</i> [2002a]	net speed/direction
<i>Danielson and Kowalik</i> [2005]	tidal harmonics
<i>Stabeno et al.</i> [2005]	net speed/direction
<i>Danielson et al.</i> [2006]	net speed/direction
Z. Kowalik (unpublished data, 2008)	tidal harmonics
www.tidesandcurrents.noaa.gov	tidal harmonics
www.ndbc.noaa.gov	sea surface elevation time series
NOAA/PMEL EcoFOCI program; see http://www.ecofoci.noaa.gov/efoci_data.shtml	moored temperature, salinity and current records at site M2
UAF Institute of Marine Science database www.ims.uaf.edu	moored current records at site F8

^aLocations of these data are shown in Figures 3a–3c.

60°N; regions 2, 4 and 6 cover the inner, middle and outer domains north of 60°N.

3.4. Sea Ice Data

[24] Sea ice concentration measurements (from the Nimbus-7 Scanning Multichannel Microwave Radiometer (SMMR) and Defense Meteorological Satellite Program (DMSP) Special Sensor Microwave/Imager (SSM/I) satellites) are from the National Snow and Ice Data Center [Cavalieri *et al.*, 1996]. These data are projected onto a 25 km grid and are available on a bidaily (1979–1987) and daily (1987–2010) basis. Bidaily data are linearly interpolated to create a daily time series for the period of observation. For spatial comparisons of the data with model results, ice concentrations from the model output were linearly regridded to match the data set resolution.

3.5. Ecosystem Indicator Time Series

[25] The first three temporal components of each EOF are correlated with various climate and biological time series to assess how resolved modes covary with potential driving mechanisms and to examine possible ecosystem responses (Table 3). Cross-correlation significance (at the 95% level)

is determined following *Pyper and Peterman* [1998]. Their method helps account for autocorrelation within each time series and results in a better determination of the effective degrees of freedom and an adjusted critical value for the cross correlation. By so doing it reduces the frequency of type I error. Records that exhibit significant linear trends are detrended prior to computing the cross correlation.

4. Model-Data Comparisons

4.1. Tides and Currents

[26] The NEP5 model-derived M_2 cotidal map is shown in Figure 4. Amphidrome locations correspond closely with those of *Kowalik* [1999] and *Foreman et al.* [2000, 2006]. Phase lines depict a westward traveling M_2 wave across the GOA and a northeastward propagating wave over the Bering Sea shelf. Amplitudes over the deep GOA waters are similar to those of *Kowalik* [1999] and the observations; however, in the western North Pacific and Bering Sea the NEP5 amplitudes are about 10 cm higher. As shown below, this difference extends onto the Bering Sea shelf, where both the tide wave and the error magnitude are amplified. Tidal elevations are largest in the semiencloded basins of Cook Inlet and Bristol

Table 2. Number of CTD and Bottle Stations for Each Region Shown in Figure 3d^a

Region	Region Number	Number of Observations at 10 m Depth	Number of Observations at 70 m Depth
$\Theta < 60^\circ\text{N}$, depth < 50 m, $\Phi > 176^\circ\text{E}$	1	1742	–
$\Theta > 60^\circ\text{N}$, depth < 50 m, $\Phi > 176^\circ\text{E}$	2	3084	–
$\Theta < 60^\circ\text{N}$, 50 m < depth < 100 m, $F > 176^\circ\text{E}$	3	4012	3480
$\Theta > 60^\circ\text{N}$, 50 m < depth < 100 m, $F > 176^\circ\text{E}$	4	777	497
$\Theta < 60^\circ\text{N}$, 100 m < depth < 200 m, $F > 176^\circ\text{E}$	5	1668	1699
$\Theta > 60^\circ\text{N}$, 100 m < depth < 200 m, $F > 176^\circ\text{E}$	6	253	263

^aRegion numbers correspond to those shown in Figures 3d and 9. Symbols are as follows: Θ , latitude; Φ , longitude.

Table 3. Time Series Employed for Correlation Analyses and Their Sources

Index	Acronym	Parameters	Source
Pacific Decadal Oscillation	PDO	first mode of North Pacific sea surface temperature variability	http://jisao.washington.edu/pdo
North Pacific Gyre Oscillation	NPGO	second mode of North Pacific sea surface elevation variability	http://www.o3d.org/npgo/data/NPGO.txt
Arctic Oscillation	AO	first mode of Northern Hemisphere 1000 mb pressure variations	http://www.cpc.ncep.noaa.gov/products/precip/CWlink/daily_ao_index/monthly.ao.index.b50.current.ascii
Pacific-North American	PNA	second mode of Northern Hemisphere 500 mb height variations	http://www.cpc.ncep.noaa.gov/products/precip/CWlink/pna/norm.pna.monthly.b5001.current.ascii
North Pacific Index	NP	sea level pressure integrated over 30°N–65°N and 160°E–140°W	http://www.cgd.ucar.edu/cas/jhurrell/indices.data.html
Integrated Ice Area	IIA	eastern Bering Sea concentration-weighted integrated ice area	<i>Danielson et al.</i> [2011]; data from http://nsidc.org/data/seaiice/pm.html
Wind direction anomaly	WDA	October–May wind direction at 60°N, 170°W	<i>Danielson et al.</i> [2011]; data from http://www-esrl.noaa.gov/psd/data/gridded/data.ncep.reanalysis.html
GAK1 CTD	GAK1T GAK1S	observed temperature and salinity anomalies over 0–20 m and 200–250 m depth strata	http://www.ims.uaf.edu/gak1/
Fresh water discharge Bering Sea ecosystem indicator time series	FWD	GOA coastal runoff phytoplankton, fish, shellfish and seabird indices including measures of condition, location, productivity, abundance, and phenology	http://www.ims.uaf.edu/gak1/ Compiled by F. Mueter (2009) http://bsierp.nprb.org/

Bay, each of which are ~200–300 km long and 30–50 m deep. Here, the wavelength of a freely propagating tide wave closely matches the resonance scale $L_R = \frac{T\sqrt{gH}}{4} = 200\text{--}250$ km, where g is gravitational acceleration, H is the average water column depth and T is the tidal period [*Gill*, 1982; *Oey et al.*,

2007]. In the northeast GOA, amplification may be due to matching of the shelf width, L_S , to the tidal, ω , and inertial, f , frequencies, and the shelf bottom slope, α (e.g., $L_S = \frac{g\alpha}{(\omega^2 - f^2)}$) [*Clarke and Battisti*, 1981]. In the northern GOA, L_S is ~100–200 km, and while the bathymetry is irregular, α is primarily

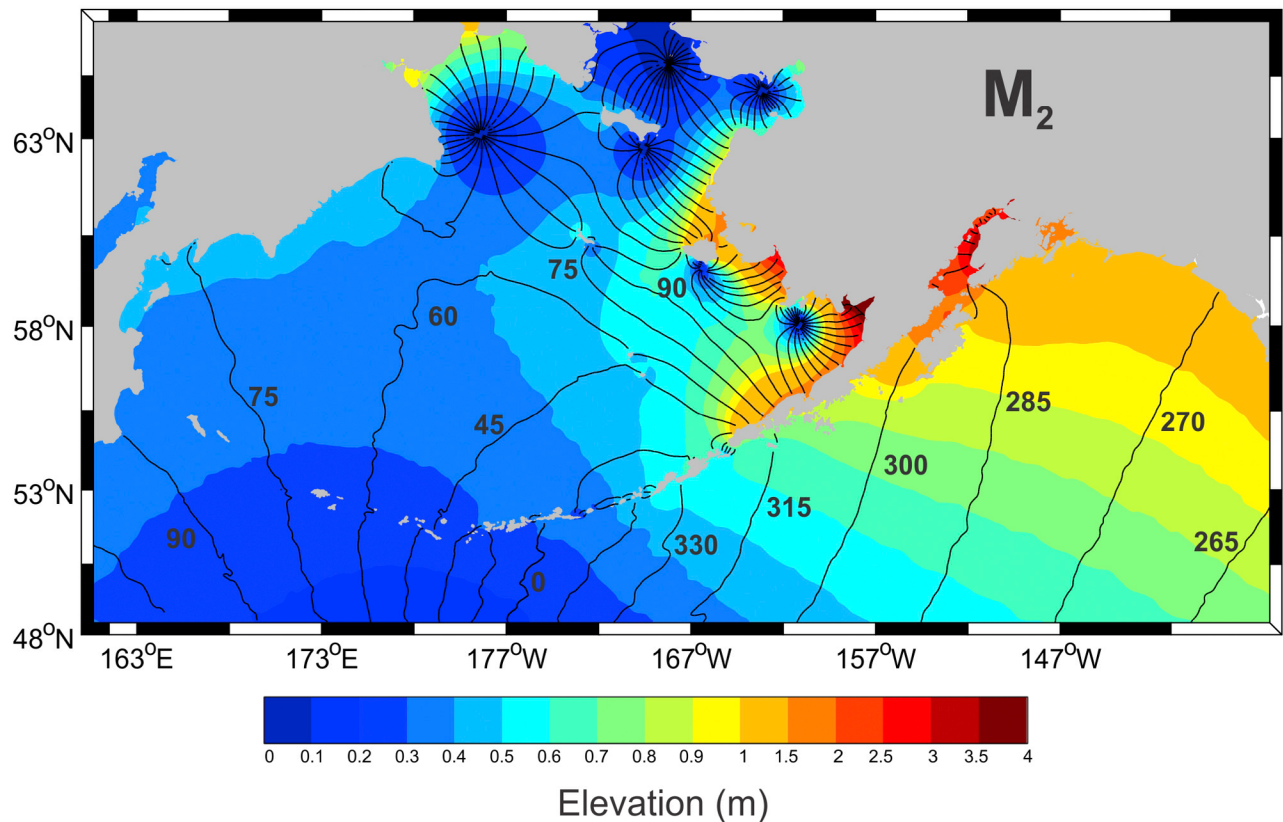


Figure 4. NEP5 model-derived M₂ cotidal chart for the Bering Sea and Gulf of Alaska. Amplitudes are contoured with color shading; Greenwich phase contours are labeled in degrees.

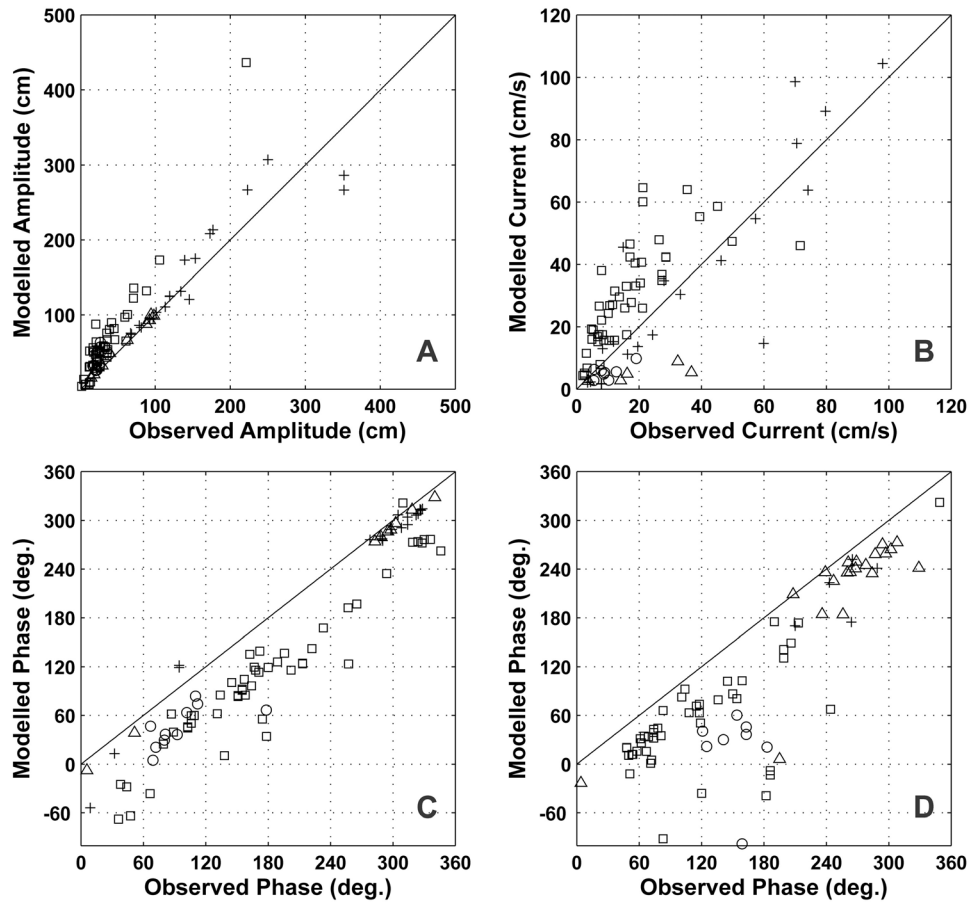


Figure 5. Comparison of model-derived M_2 tidal elevation and current analyses at the locations of the moored and coastal tide stations plotted in Figure 3: (a) tidal elevation, (b) tidal current ellipse semi-major axis magnitude, (c) elevation phase, and (d) current ellipse phase. Solid lines depict the 1:1 ratio. Symbols denote stations located in different regions: squares are from the Bering shelf, triangles from the deep North Pacific and Gulf of Alaska, pluses from the GOA shelf, and circles from the deep Bering basin and Aleutian Islands.

between 10^{-3} and 10^{-4} and the lower portion of this range satisfies the resonance criterion.

[27] Figures 5a and 5c compare the M_2 tidal elevations and phases from harmonic analyses of the model results and observations at the sites shown in Figure 3b. The median amplitude error expressed as a fraction of the observed amplitude is 30% when all locations are considered; this error is 80% when only the Bering shelf stations are included. Comparisons to Kowalik [1999] suggest that this overestimate is likely due to insufficient damping of the M_2 wave as it crosses the Aleutian Island chain. Errors in model bathymetry (smoothness; cross-sectional area of passes) and/or parameterization of bottom friction are likely causes for the excess flux of energy to the Bering Sea basin. The points clustered nearly on the 1:1 phase line at $\sim 300^\circ$ consist primarily of the deep-ocean stations south of the Aleutian Islands, indicating that the model accurately reproduces the phase of the tide wave in the northern North Pacific. However, north of the Aleutians and over the Bering shelf, the model tidal wave phase is retarded relative to the observations. For the Bering shelf, the modeled M_2 tide lags the observations on average by about 60° (2 h).

[28] Figures 5b and 5c compare harmonic analyses of current observations and the model's depth-averaged currents located at the closest grid cell to the observations. The semimajor axis of the current ellipses are evenly distributed about the 1:1 line although the relative scatter is greater than for the elevations. As with the tidal elevations, the Bering shelf shows larger errors than the GOA shelf. Because the tidal current timing is strongly dependent upon the elevation phase, the modeled tidal current phase also lags the observations, but on average by ~ 30 degrees. This difference may be partially explained by the proximity of historical current meters to the bottom, which were often deployed within the M_2 bottom boundary layer (BBL). Hence the observations may both underestimate the water column average M_2 semimajor axis magnitude (Figure 6a) and slightly advance the phase (Figure 6d).

[29] To examine the vertical structure of the tidal currents, Figure 6 compares modeled and observed ellipse parameters from mooring site F8, located just south of St. Lawrence Island. The observations are from a moored ADCP, which misses the water column's uppermost 5 m and bottommost 7 m. In addition, the water column depth at site F8 is 50 m,

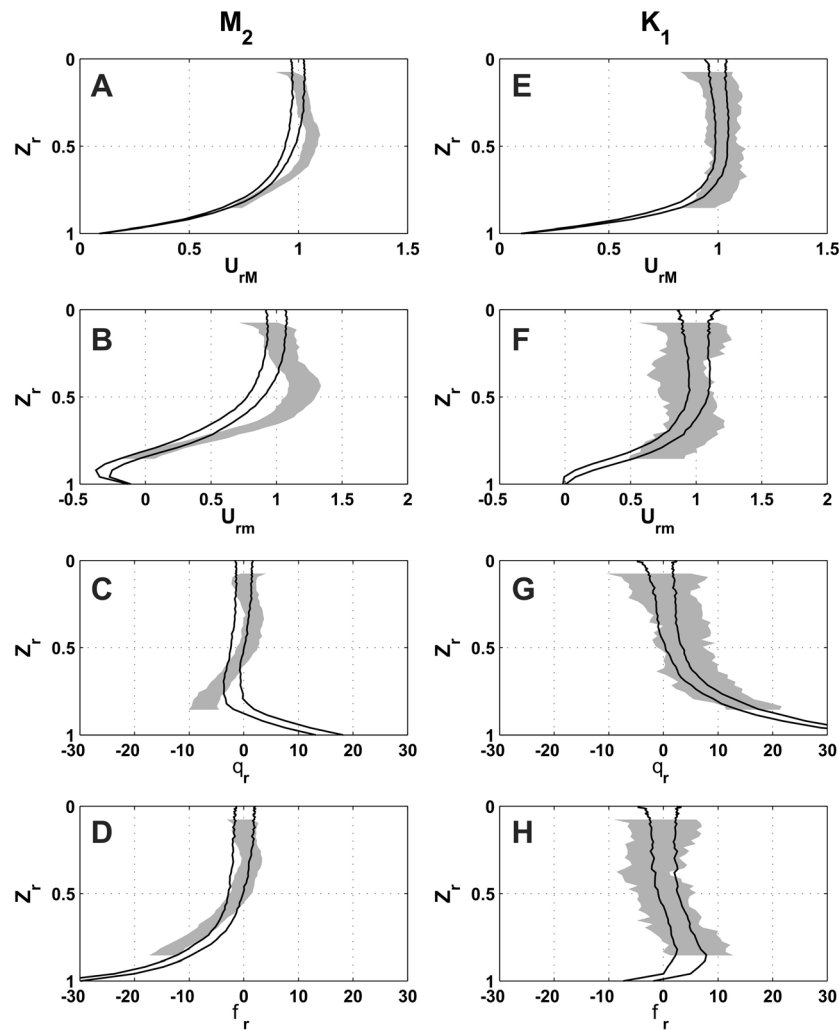


Figure 6. Vertical structure of the M_2 and K_1 tidal ellipse parameters. Depths (Z_r) and tidal parameters (U_{rm} , semimajor axis; U_{rm} , semiminor axis; θ_r , inclination; ϕ_r , Greenwich phase) are scaled as described in section 4.1. Shading and lines bound the 95% confidence limits on the observed and model ellipse parameters, respectively.

whereas the depth at the closest model grid point is 46 m, so we expect a 4 m offset between the two profiles. To focus attention on the vertical structure rather than differences in magnitude, phase or bottom depth, the ellipse parameters in Figure 6 are scaled as follows. Water column depths (Z_r) are scaled between 0 (sea surface) and 1 (seafloor). At $Z_r = 0.10$, amplitudes are scaled to unity and the phase and inclination parameters are offset to 0° . The M_2 BBL is thicker than the K_1 BBL, because the M_2 (K_1) frequencies are on opposite sides of the inertial frequency resulting in different dynamics between the subinertial and superinertial waves [Defant, 1960; Prandle, 1982]. Both the observed and modeled M_2 ellipses rotate clockwise (CW) in the upper portion of the water column and counter-clockwise (CCW) near the seafloor. For the K_1 tide, the CW component dominates everywhere. The observed M_2 profile has a slight middepth maximum owing to tidal enhancement near the pycnocline during the summer when the water column is strongly stratified [Danielson and Kowalik, 2005]. The NEP5 model does

not reproduce this feature, suggesting that the model may not contain sufficient late summer stratification near this site. The model and observed 95% confidence ranges overlap throughout the observed depth range for all of the K_1 ellipse parameters. The confidence limits also overlap for the M_2 parameters except at middepth for the currents and in the lower third of the water column for the orientation and phase angles.

[30] Rotary spectra [Mooers, 1973] derived from the 10 and 50 m depth levels at mooring site M2 are shown in Figure 7. The spectra were calculated from nonoverlapping windows and then smoothed with a five point moving average to highlight the tidal frequencies.

[31] In the short-period (10–30 h) portion of the spectrum, the 95% confidence limits of the model and observed spectra overlap for both depths except for the counterclockwise (CCW) component at 10 m depth. The moored spectrum flow is strongly polarized in the CW component for these periods, implying that motions are nearly circular. In contrast, the

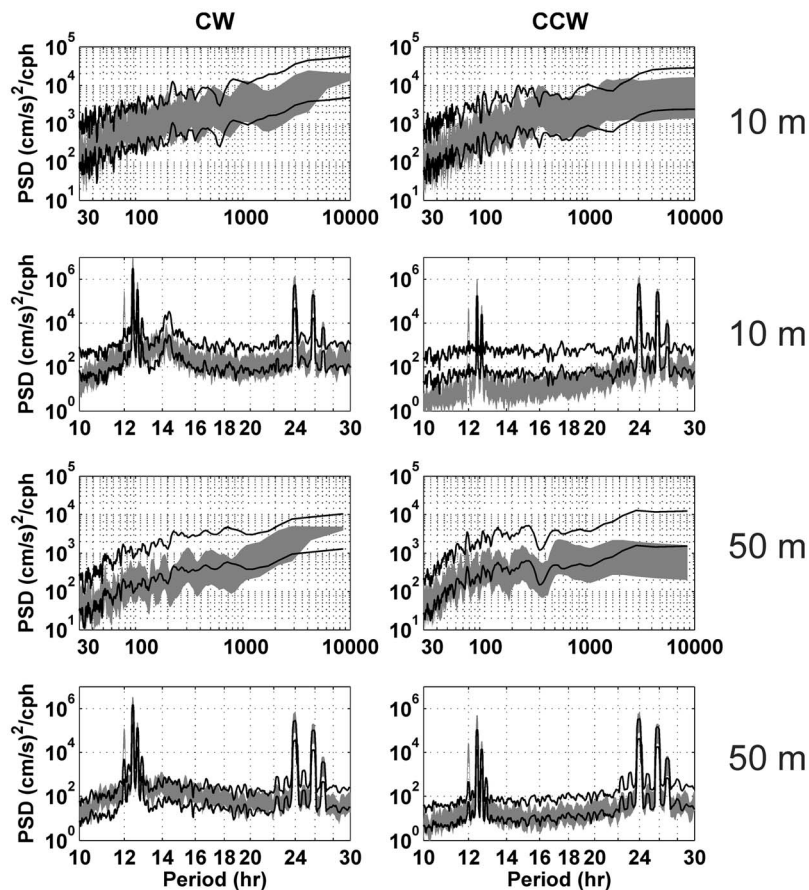


Figure 7. Power spectra density (PSD) at 10 and 50 m depths at mooring site M2 from observations (shading) and the model (lines). Shading and lines delimit the 95% confidence limits. Short-period (10–30 h) and long-period (>30 h) portions of each spectrum are shown separately. (left) The clockwise (CW) and (right) counterclockwise (CCW) rotating components are shown.

magnitudes of the model CW and CCW components are similar to one another, indicating that the model’s high-frequency motions are overly elliptical and that in this band the model contains too much kinetic energy. The model’s high-frequency bias is not present at 50 m depth. In both the observed and model spectra the inertial peak is well defined at 10 m depth but is barely discernable at 50 m depth.

[32] The long-period (>30 h) observed and model spectral envelopes have similar variations and the confidence limits overlap across this frequency range. While the 10 m observed and model spectra are nearly indistinguishable from one

another, the modeled 50 m spectrum is consistently larger than the observed; it is larger by about one half the observed confidence limit range. Both the observed and modeled spectra have many corresponding peaks and troughs and, importantly, similar background noise levels. We conclude that the spectral character of the subtidal model currents at this particular location is in general agreement with the observed spectra.

[33] Our final comparison between model-derived and observed currents is based on mean current vector magnitude and direction records from the sources in Table 1.

Table 4. Statistics of Current Meter Vectors Compared With Colocated (in Space and Time) Model-Derived Vectors^a

Region	N	L (months)	$O_{\text{mse}}:O$ (%)		$ O-M :O$ (%)		Mean $ O $ (cm s^{-1})	$ O-M $ (cm s^{-1})		$\Delta\theta$ (deg)	
			Mean	Median	Mean	Median		Mean	Median	Mean	Median
64.5 < latitude	18 (1)	5.7	14	14	29	30	24.6	7.4	5.7	10	10
61 < latitude < 64.5°N	47 (14)	5.0	55	39	54	52	5.2	2.8	1.7	55	30
55 < latitude < 61°N	10 (10)	7.4	50	45	76	30	2.5	1.1	0.9	77	46
Latitude < 55°N	29 (4)	18.8	80	76	79	81	16.1	10.8	8.7	75	79

^aRegion denotes latitude band of observations. N, number of current meter records within the latitude band and, in parentheses, the number of records with 95% confidence limits on the mean speed; L, mean record length in months; $O_{\text{mse}}:O$, magnitude of error represented as a fraction of the observed mean speed; $|O-M|:O$, magnitude of observed-model speed difference represented as a fraction of the observed mean speed; $|O|$, mean observed speed; $|O-M|$, magnitude of observed-model speed difference; and $\Delta\theta$, magnitude of mean vector direction difference. Values for $O_{\text{mse}}:O$ and $|O-M|:O$ reflect quantities that are only available for the subset of stations with error estimates.

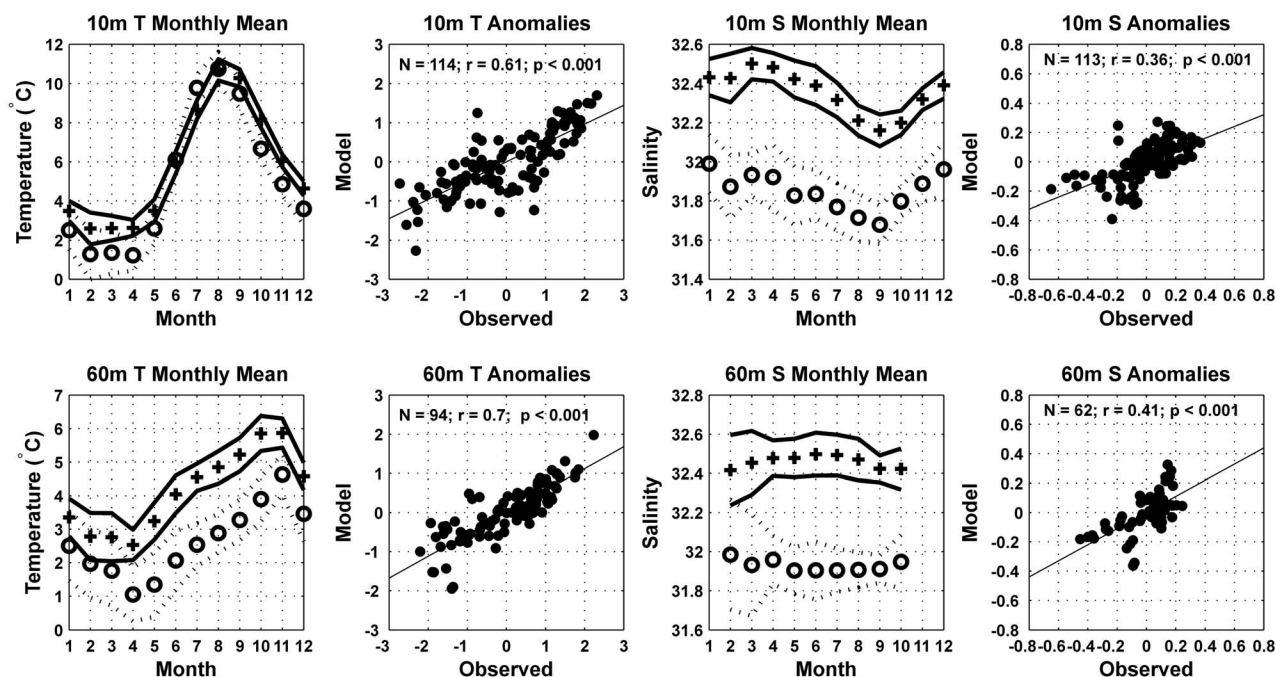


Figure 8. Mooring site M2 1995–2005 annual cycle of temperature and salinity monthly means and anomalies from (top) 10 m and (bottom) 60 m depth. Model (mooring) data are plotted with pluses (circles), and solid (dashed) lines indicate the 95% confidence interval upon each monthly mean. Notation indicates the number of months (N), correlation coefficients (r), and p values for $N-2$ degrees of freedom. Straight lines depict the least squares best fit.

Corresponding model results were generated from detided and then daily averaged currents at the model grid cell closest to the deployment location. The model currents were aligned in time and depth with the observations. Table 4 shows the relation between the hindcast and observed mean velocity records, grouped into zonal clusters.

[34] The mean flow over the Bering shelf is generally weak ($<10 \text{ cm s}^{-1}$) and oriented along isobaths toward the north. Flow reversals are common [Schumacher and Kinder, 1983] so that many of the mean observed (and modeled) low-frequency vector components are not statistically different than zero. Such large variability renders statistical comparisons of mean velocity estimates difficult and results in the large ratios of mean speed to (1) the error magnitude and (2) the model/observed speed difference (Table 4). Strong ($\sim 25 \text{ cm s}^{-1}$) northward currents in Bering Strait are the exception: here the mean RMSD is only 14% of the mean speed and typical errors are within 30%. For observations reported with 95% confidence limits on the current speed, the model mean speed falls within these limits for $\sim 40\%$ of the records. Away from the Aleutian Islands and Bering Strait (Table 4), mean speeds are small ($2.5\text{--}5.2 \text{ cm s}^{-1}$) and the average model speeds are typically within 3 cm s^{-1} of those observed. With a few exceptions, mean differences in speed (represented as a percentage of the observed speed) are similar to the error estimates of the mean observed speed. Differences in current direction range between 10° and 79° . The largest discrepancy is in the southernmost latitude band, along the Aleutian Islands, where narrow passes, complex bathymetry, and strong tidal currents occur. The two northern most comparison

ensembles show closest agreement in both the magnitude and direction.

[35] In summary, we find that the model somewhat overestimates the tidal elevation amplitude and current magnitude over the Bering shelf although geographic distribution of these parameters and the vertical structure of the currents are reasonably reproduced. The spectral character of the model currents generally follows that of the observations, although the modeled tidal and subtidal currents generally have greater kinetic energy. Given the large synoptic variability with respect to the mean, it is difficult to make meaningful comparisons to the available suite of published mean velocity vector statistics. Bulk comparisons indicate that the model performance varies in space and we have at least bounded the range of probable errors in the modeled mean flow. Fronts and stratification also affect the shelf response to external forcing, so modeled currents also depend upon the model's ability to reproduce the shelf thermohaline structure.

4.2. Temperature and Salinity

[36] We next compare the temperature and salinity fields, considering first the long-term mooring records from mooring site M2 (Figure 1) and then shipboard hydrography. Figure 8 shows the observed annual cycle of temperature and salinity at M2 depicted by the monthly means and their monthly anomalies computed between 1995 and 2005. Observed and modeled temperatures at 10 and 60 m depth vary in phase and have identical annual amplitudes. The only significant (at the 95% confidence limits) differences between temperatures at 10 m depth occur in April, October

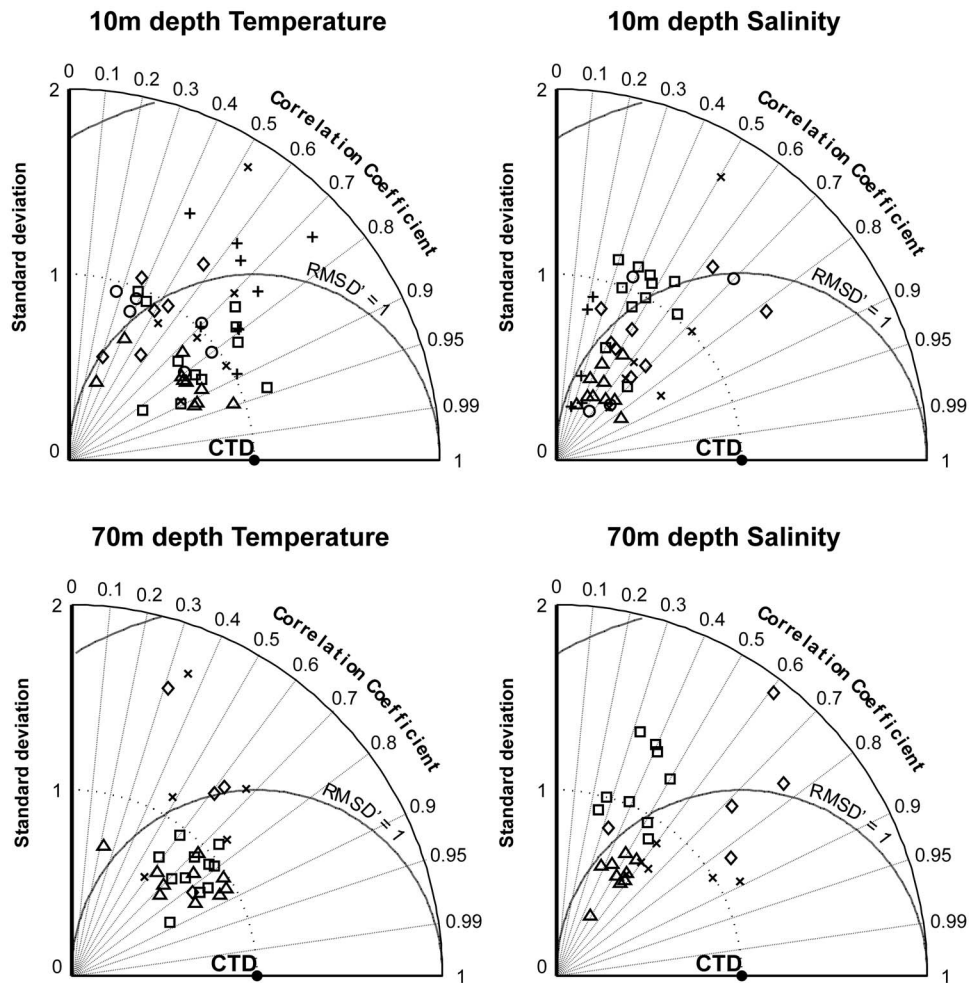


Figure 9. Temperature and salinity Taylor diagrams for the 10 and 70 m depth levels. Symbols correspond to the regions listed Figure 3 and listed in Table 1. Regions 1, 2, 3, 4, 5, and 6 are associated with pluses, circles, squares, diamonds, triangles, and crosses, respectively. Each point represents month-specific summary statistics for the cases where $p < 0.05$ and the parameters fall within the ranges of the diagrams (a few points with large RMSD fall off the figures). The point marked CTD represents the observational reference with $\text{RMSD}' = 0$, $r = 1$, and $\sigma = 1$.

and November. The higher temperatures in the two fall months are due to a delayed onset of fall cooling and, as shown below, this leads to a corresponding delay in model sea ice growth. The 60 m model temperatures are $\sim 1\text{--}2^\circ\text{C}$ warmer than observed from April through November. Observed 60 m temperatures do not increase from October to November however in the model fall temperatures continue to rise through November. Both near-surface (10 m) and deep (60 m) model salinities are consistently ~ 0.5 less than observed (with nonoverlapping error bars), but observed and modeled 10 m salinities vary in phase and have the same annual amplitudes (January to September decrease of $\sim 0.3\text{--}0.4$). In contrast, the deep model salinities show a February to June increase of ~ 0.1 while over the same period the observed salinities decrease by the same amount. The error bars show that neither of these seasonal trends is statistically significant.

[37] Monthly anomaly comparisons in Figure 8 address the model's ability to reproduce seasonal and interannual variability in the thermohaline fields. At the 10 m (60 m) depth

level, the model reproduces 37% (49%) of the observed temperature variability. Salinity anomalies are less accurately hindcast: the model captures 13% (17%) of the observed variability at the 10 m (60 m) depths. These results are consistent with our expectations: thermodynamic balances are more straightforward to accurately compute; fresh water variability on the shelf is tied to complex freezing and thawing processes, surface fluxes, coastal river discharges and cross-shelf exchanges. River discharge in particular is not accurately implemented in NEP5 because the prescribed fluxes do not include seasonal or interannual variability.

[38] To examine temperature and salinity variability more broadly across the shelf, we assembled historical CTD and discrete bottle measurements for six Bering shelf subregions (see Table 2 and Figure 3d). We selected the 10 m (near surface) and 70 m (subsurface) depth levels for comparison and computed statistics on the basis of each calendar month separately in order to investigate interannual rather than seasonal variability (Figure 9).

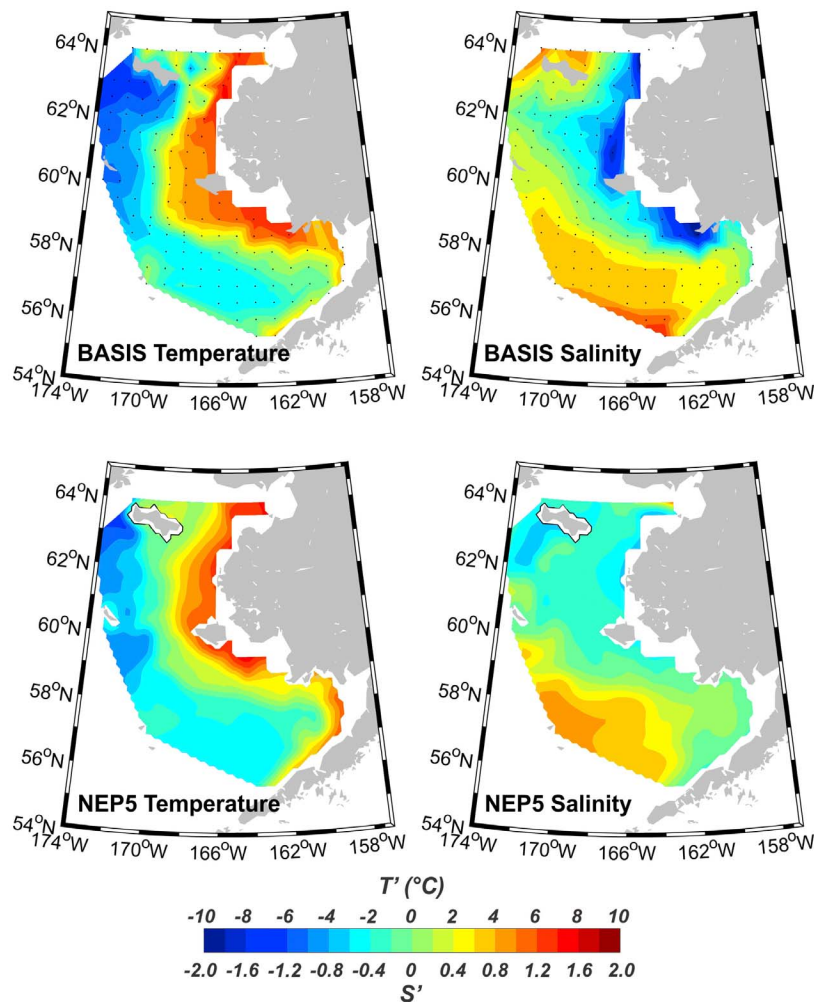


Figure 10. Near-bottom contours of (left) T' and (right) S' from (top) CTD data and (bottom) model hindcasts, where $T' = T - T_{\text{mean}}$ and $S' = S - S_{\text{mean}}$. BASIS CTD data were collected between 14 August and 30 September 2004; model results are the 2 month average of the August and September 2004 fields. BASIS samples were collected at the locations marked with black dots.

[39] As with the moored records, the temperature comparisons are more favorable than those for salinity. More than one half of the 10 m temperature comparisons in Figure 9 lie within $0.7 < r < 0.95$, $\text{RMSD}' < 1$ and $0.5 < \sigma < 1.5$. Temperature comparisons at 70 m depth mostly fall within $0.5 < r < 0.9$, $\text{RMSD}' < 1$, and $0.6 < \sigma < 1$. For both depths, many of the salinity comparisons lie within $\text{RMSD}' < 1$ and $0.3 < r < 0.7$. The model exhibits some differences in performance among regions: at 10 m depth, for example, region 5 (outer shelf, south of 60°N) temperatures agree best with the observations in most months, while in region 1 (inner shelf, south of 60°N) temperatures have the largest RMSD' . Salinities in all other regions occupy a similar range of correlations as those in region 3 (midshelf, south of 60°N) however the standard deviations in region 3 are closest to unity. These analyses are consistent with the comparisons made with the moored temperature and salinity records: the model has some ability to hindcast both temperature and salinity fields at surface and subsurface depths and has more skill with the thermal field than with salinity. The model exhibits slightly better performance in some regions than in others.

[40] Our analyses of hydrographic data focused on the model's ability reproduce interannual variability, however spatial variability within each region impacts our results. We can estimate the magnitude of this by comparing results from region 3 to results from mooring site M2 (containing temporal variability only). Within region 3 we find correlations (r) mostly between ~ 0.7 and 0.9 at 10 m depth (Figure 9) versus $r = 0.61$ computed from the moored mooring data (Figure 8). These comparisons suggest that spatial autocorrelations improve the 10 m temporal correlation by about 0.1 – 0.3 ; at the 70 m depth level the correlation improves by about 0.1 . Region 3 salinity correlations are only slightly smaller ($\Delta r < 0.1$) than those at M2 suggesting that any spatial autocorrelations have minor influence on the salinity results in Figure 9. The correlations will also reflect the extent that spatial variability across each region represents an appreciable fraction of interannual variability. This is most apt to be the case in the nearshore regions during late summer and early fall when horizontal gradients are largest.

[41] Using the 2004 BASIS program CTD survey, we compare the in situ near-bottom temperature and salinity

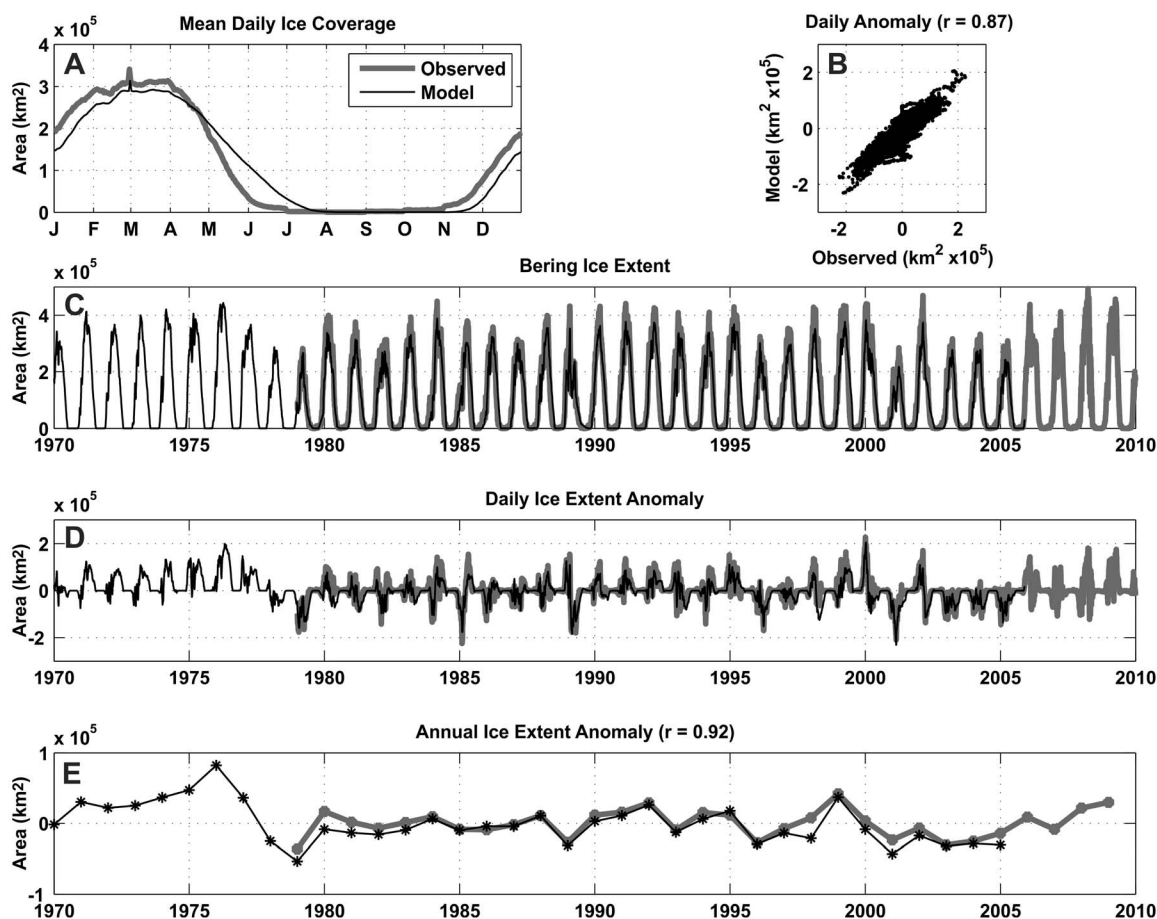


Figure 11. Bering Sea integrated ice extent and anomalies from the model and passive satellite observations integrated over the eastern Bering Sea: (a) daily mean annual cycle of ice extent, (b) daily anomalies, (c) time series of total ice extent, (d) daily anomalies, and (e) annual anomalies. Observations are plotted in gray, model results in black.

fields with those hindcast by the model (Figure 10) after linearly interpolating and truncating the model output to match the BASIS grid, and subtracting the mean value from each field. This latter transformation highlights spatial gradients rather than the offsets found with the moored record comparisons above. We find that the spatial structure of the hindcast temperature field matches the observed pattern with the exception of the cold tongue south of St. Lawrence Island. This tongue extends to the eastern reaches of the island in the observations but not in the model, suggesting that eastward flow observed on the south side of St. Lawrence Island [Schumacher *et al.*, 1982; Danielson *et al.*, 2006] is not fully reproduced in the model. While the model shows higher-salinity waters in the midshelf region, it does not capture the pronounced nearshore freshening that extends from Kuskokwim Bay to Norton Sound. This discrepancy may be a consequence of the time-invariant coastal discharge used in the model. Bering Sea river discharges exhibit strong seasonal variability because of the annual freeze-thaw cycle. Incorporating this variability in future models should lead to more realistic shelf salinity fields. The shelf salinity is also modulated by ice melting and formation processes, which we consider next.

4.3. Sea Ice

[42] In this section, we compare model ice concentrations to measurements made by passive microwave satellites. We form daily averages of ice extent weighted by percent concentration for the period January 1979 to November 2005 by integrating over the region east of 170°E and south of 66°N which represents most of the Bering Sea area subject to seasonal ice cover.

[43] The mean annual cycle of ice cover (Figure 11a) indicates that the model closely reproduces the observed annual amplitude. Although the modeled spring ice retreat onset coincides with the observed, the model retreat rate is considerably slower. This discrepancy may be because the model currently lacks the ability to alter the ice albedo (and melt rates) owing to wet ice conditions, melt ponds, and ice algae or debris within the ice [Curry *et al.*, 1995]. In addition, passive satellite measurements have difficulty in distinguishing between open water and wet or subsurface ice [Comiso *et al.*, 1997] so the satellite observations likely underestimate the spring ice extent. Consistent with the delayed onset of fall water column cooling noted in section 4.2, fall ice development in the model lags the observations by ~ 3 weeks, although growth rates thereafter are comparable to observed.

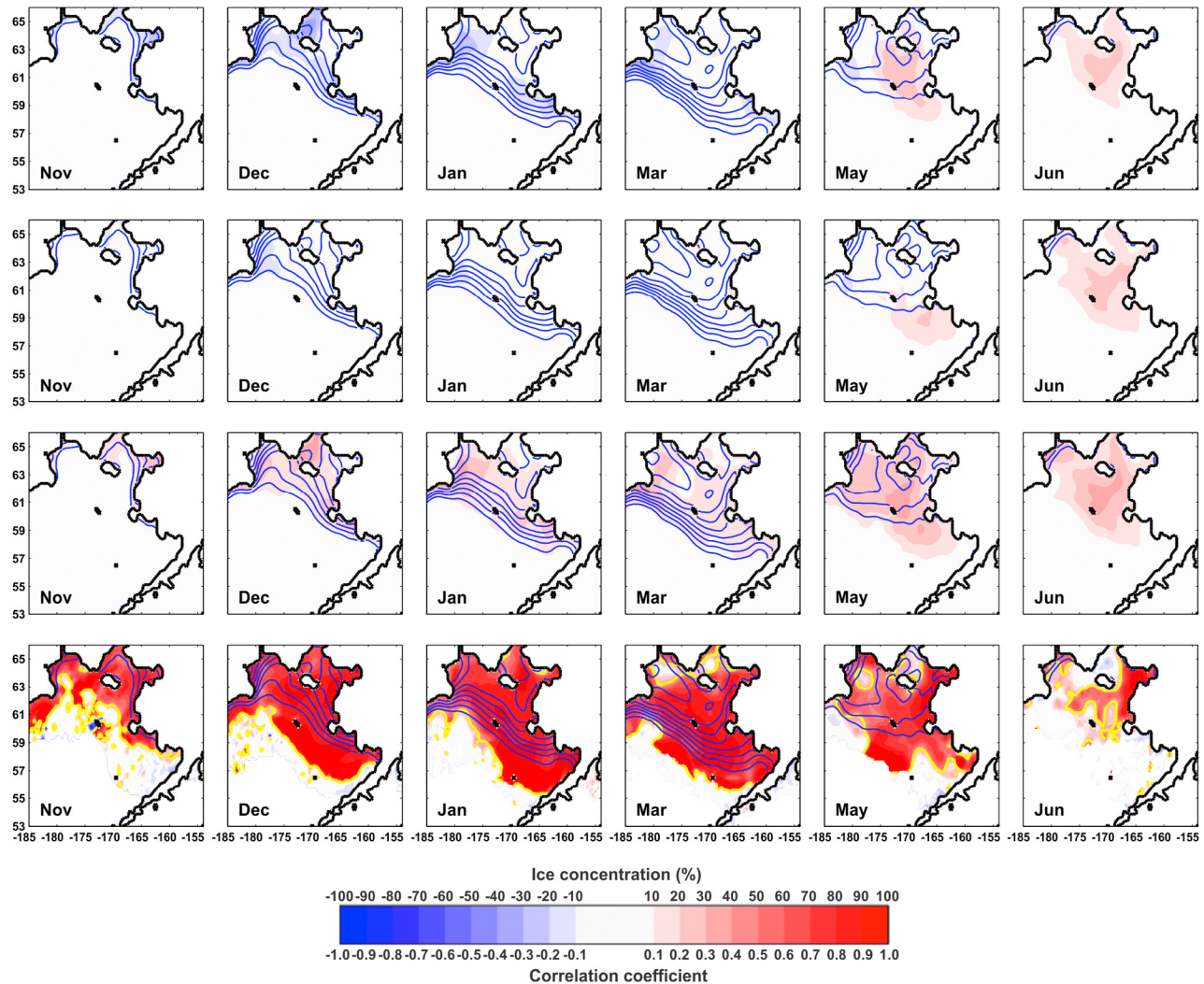


Figure 12. Observed mean monthly ice concentration is given with blue contours in all rows for the months indicated. Color shading depicts the mean model minus observed ice concentration difference (first row), standard deviation of the model minus observed difference (second row), model minus observed RMSD (third row), and the model:observed cross correlation (fourth row). Shading increments occur at integer multiples of 10% for the first three rows and at integer multiples of 0.1 for the cross correlations. Yellow contours bound regions where the correlation is significant at the 95% level.

Comparison of the daily ice extent anomalies (see Figures 11b and 11c) suggests that the model captures much of the integrated synoptic variability, accounting for 75% of the observed daily variance ($r = 0.87$, $p < 0.001$). The model reproduces 85% of the observed interannual variance ($r = 0.92$, $p < 0.001$) and there is no discernible trend in either the observed or modeled annual ice extent anomaly time series (Figure 11e).

[44] Spatial distributions of mean monthly sea ice concentration over the eastern Bering Sea are plotted with blue contours in Figure 12. Figure 12 (first row) shows that model-observed differences in concentration are $<10\%$ over most of the analyzed domain. Exceptions are in the Gulf of Anadyr and Chirikov Basin for December and March where the model underestimates ice concentrations by up to 30%. The delayed onset in freeze-up noted above is primarily due to the underestimated concentrations here, suggesting that the

model may generate too much polynya and/or lead area in early and late winter. Overestimates of ice extent in May and June are mostly confined to the central northern shelf. Standard deviations of ice concentration (Figure 12, second row) are generally within 10% of each other with the exception of higher model variance south of Nunivak Island in May and across the northern shelf in June; both a consequence of delayed melt. Absolute (RMSD) error between the model and observations (Figure 12, third row) is typically in the range of 10–20% through the winter; however, in May and June extensive regions with concentration errors of 20–40% persist. The correlation maps (Figure 12, fourth row) show that for most months, the region of significantly correlated (at the 95% level) variability greatly exceeds the area bounded by the 10% concentration contour. This verifies that when the ice edge is located far south (or north) of its mean position, the model captures this signal. Correlations

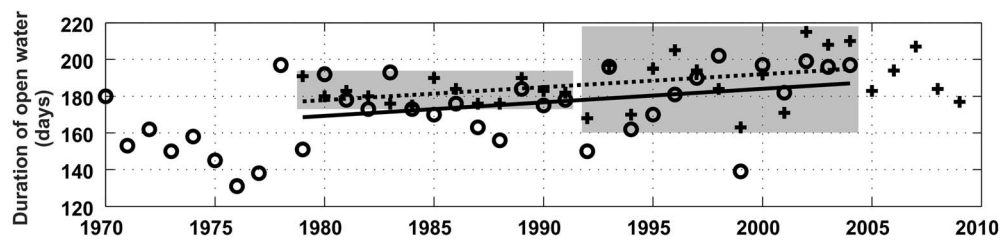


Figure 13. Time series of the annual number of ice-free days. Straight lines depict the least squares best fit linear trend to each series for the period of overlap (1979–2004). Observational (model) results are represented by pluses and the dotted line (circles and solid line). The range of the observed open water season is shaded separately for the 1979–1991 and 1992–2004 time periods.

weaken in the Gulf of Anadyr and Chirikov Basin, perhaps because of this region’s proximity to the northern model boundary, where advection influences are strong and the northern boundary condition artificially specifies a constant northward transport.

5. Discussion

5.1. Model Strengths and Weaknesses

[45] Our comparisons focused on the NEP5 model’s skill at hindcasting observed variability of the thermohaline, sea ice and circulation fields of the eastern Bering Sea shelf. On monthly to annual time scales, we find that the model’s primary strengths include its ability to reproduce 85% of the interannual variability in the integrated sea ice extent (Figure 11) and to account for up to nearly 50% of the variance in monthly temperature anomalies (Figure 8). On tidal and synoptic time scales, the model reproduces with significant skill the horizontal (not shown) and vertical structure of tidal currents (Figure 6) and the frequency distribution of current kinetic energy (Figure 7) although the model has somewhat greater kinetic energy overall (see Figures 5 and 7).

[46] The model less accurately hindcasts the sea ice extent during the melt season and the monthly salinity anomalies (see Figures 11 and 8). However, errors in the salinity field are not particularly surprising given the prescribed coastal discharges and the large fresh water sources for the Bering shelf including the Yukon River and the integrated GOA discharge [Royer, 1982] a significant portion of which enters the Bering shelf [Stabeno *et al.*, 2002a; Weingartner *et al.*, 2005; Aagaard *et al.*, 2006]. The GOA discharge is particularly difficult to capture with a 10 km resolution given the complex orography and coastline of this shelf. Improvements to the model are presently underway with respect to a more realistic coastal discharge and for the northern boundary condition. These changes, along with the wave-mixing parameterization of Hu and Wang [2010] may improve the modeled stratification for the shelf. Notwithstanding these shortcomings, in its present form the model does allow us to examine aspects of the interannual variability in sea ice, temperature and salinity over the Bering Sea shelf.

5.2. Trends in the Annual Duration of Ice-Free Waters

[47] Danielson *et al.* [2011] quantified an increasing trend in the duration of the 1979–2009 open water season, defined as the last spring day (first fall day) that the eastern Bering Sea concentration-weighted integrated ice area falls below (rises above) 50,000 km² (the IIA index in Table 3). The model

results allow us to extend this analyses to 1970 (Figure 13), nearly a decade longer than the modern satellite record. The model hindcast results suggest that there was a step change in open water duration that coincided with the mid-1970s “regime shift” [Minobe, 1999; Mantua *et al.*, 1997; Stephens *et al.*, 2001]. This result is consistent with reports that the early to middle 1970s was a period of heavy Bering Sea and western Arctic ice cover [Gibson and Schullinger, 1998; Niebauer, 1998]. Over the 1979–2004 period of overlap between the model and observations we find a marginally significant increasing trend in the length of the open water season in both the observed (7.4 days/decade, $r = 0.40$, $p = 0.041$) and the hindcast (7.1 days/decade, $r = 0.33$, $p = 0.095$) time series. The model’s mean open water season is 8.5 days shorter than that observed, a result of the model’s apparent inability to melt ice fast enough in the late spring and early summer (Figure 11).

[48] We also observe a change in the variance of open-water season duration between the first half (1979–1991) and the second half (1992–2004) of the record. The observations indicate increase in variance from 32 days² to 306 days² between the two periods and the model variance increases from 151 days² to 418 days². Given the large interannual variability in the duration of the ice-free waters since 1992, it appears that Bering shelf is presently within a state characterized by higher year-to-year variability. This increased variance may imply increased ecosystem variability by altering spring production dynamics that propagate through seasons and across trophic levels [e.g., Hunt *et al.*, 2002].

[49] The hindcast open water season duration for 1970–1978 (corrected for the 8.5 day offset) combined with the 1979–2009 observational record results in a time series with a highly significant 1970–2009 trend of 6.8 days/decade ($r = 0.52$, $p < 0.001$). This trend will not persist because the ice growth season can be truncated only so far given winter ocean-atmosphere heat loss at this latitude. The model also indicates thinning ice by winter’s end from 1970 to 2005; the trend is not significant.

5.3. Temperature and Salinity Variability

[50] Near-surface shipboard CTD data collected by the BASIS program depict an apparent anticorrelation in the cross-shelf salinity field, while the cross-shelf temperature field exhibits an in-phase relation [Danielson *et al.*, 2011]. Selecting the grid point closest to M2 as our reference, we perform a similar analysis using monthly fields and find distinct patterns in each of the model-generated parameters (Figure 14). The in-phase temperature relation reflects the

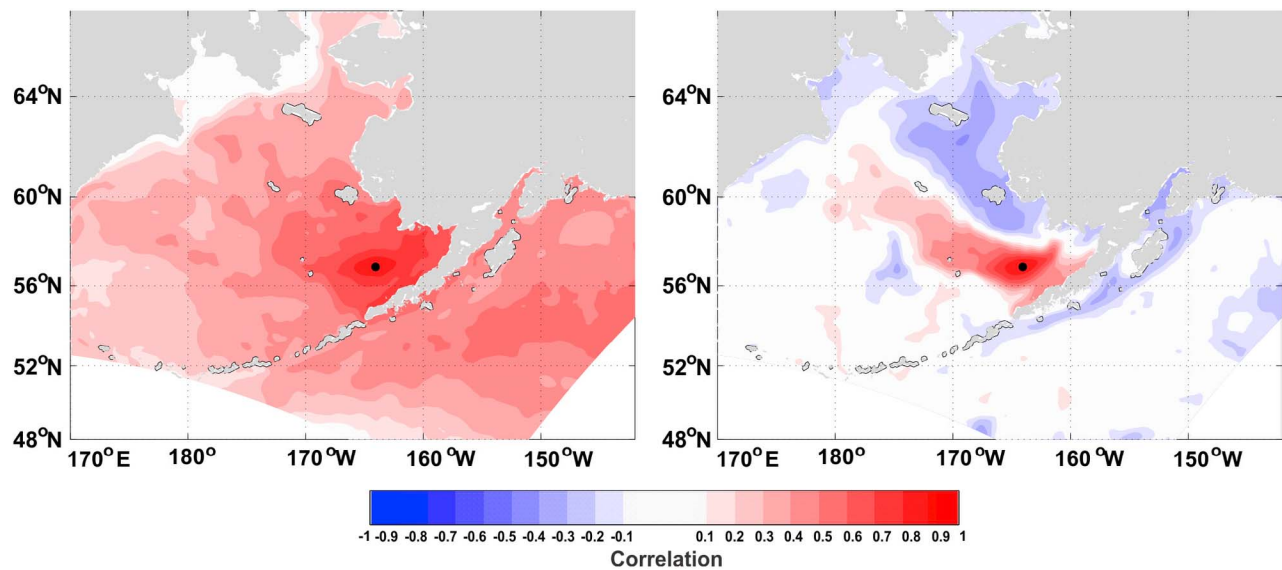


Figure 14. Correlation maps of 1970–1985 monthly average 0–20 m (left) temperature and (right) salinity time series. The reference point is located near mooring M2, denoted with a black dot.

long (>1000 km) length scales associated with atmospheric forcing (e.g., the Aleutian Low). *Danielson et al.* [2011] attribute the cross-shelf salinity pattern to the redistribution of fresh coastal waters by the winter (October to May) wind field; the signal was significantly correlated with the previous winter's cross-shelf Ekman transport and the winter wind direction anomaly (WDA index in Table 3) computed at 60°N, 170°W. The salinity correlation pattern depicted in Figure 14 is similar to that found by *Danielson et al.* [2011] however the boundary between the two opposing phases is farther offshore in the model results. Thus, the model pattern less clearly signifies a coastal and middle shelf water mass exchange phenomena but may instead reflect ice dynamics: in years of extensive ice more brine is released in the north and more melt occurs in the south.

[51] On the basis of the monthly average model fields, we compute EOFs for annually averaged temperature (T) and salinity (S) anomaly fields using every fourth model grid point over the Bering Sea and northern GOA. We consider the first three EOF modes from upper (U; 0–20 m) and lower (L; 40–100 m) depth layers. To remove the annual cycle and to minimize spatial biases, the records at each grid point was normalized into a standard monthly anomaly time series having unity variance and zero mean. Seasonal EOFs were similarly calculated and yielded results nearly identical to those described below. Following *North et al.* [1982], all modes discussed are fully resolved. Principal components are correlated to the time series listed in Table 3.

[52] Within the upper layer EOFs (Figure 15), the first temperature mode (mode T1U) accounts for 47% of the total variance, and modes T2U and T3U account for 14% and 6%, respectively. The T1U mode is in phase over the region considered and is significantly and positively correlated ($r = 0.59$) with the PDO (Table 5), suggesting the influence of large-scale atmosphere-ocean heat fluxes and the associated sea level pressure fields. This notion is consistent with the negative correlation ($r = -0.67$) between T1U and the IIA index, which depends on the regional winds [*Overland and*

Pease, 1982]. T1U is also correlated (but less strongly) to the North Pacific (NP) ($r = -0.36$) and the (WDA) ($r = 0.44$) indices, which are influenced by the position and strength of the Aleutian Low [*Trenberth and Hurrell*, 1994; *Danielson et al.*, 2011].

[53] EOF T2U depicts an out-of-phase relationship between the northern GOA/southeastern Bering Sea and the western Bering basin/southwestern GOA. The pattern is positively correlated with the near-bottom (200–250 m) temperature at GAK1, the NPGO, the PNA and the GOA discharge record. The NPGO, the second mode of sea surface height variability in the North Pacific Ocean, is related to the sea surface elevation gradient between the North Pacific subarctic and subtropical gyres [*Di Lorenzo et al.*, 2008]. Positive anomalies in the NPGO imply enhanced transport within the North Pacific Current and the GOA gyre [*Di Lorenzo et al.*, 2008]. This gyre advects relatively warm waters into the GOA and so the NPGO index is positively correlated with temperature anomalies at station GAK1. The southeastern Bering Sea shelf is in phase with the GOA shelf and basin for mode T2U, presumably reflecting the advective or atmospheric connections between these two regions.

[54] EOF T3U exhibits positive phase over the northern Bering basin and GOA shelf and negative phase over the northern Bering shelf/southern Bering basin. Although it is unclear what establishes the spatial structure of this mode, it is correlated with two winter processes that are functions of the location and strength of the Aleutian Low: the winter (October–May) wind direction anomaly (WDA) and the ice extent index. The WDA index is also correlated with the summer's end central shelf salinity anomaly and may reflect interannual variability in the winter surface circulation [*Danielson et al.*, 2011]. EOF T3U suggests that the southern Bering shelf and GOA shelf may be linked by advective processes that are confined to the outer Bering shelf and shelfbreak, unlike the signal of T2U for which the positive phase extends across all of Bristol Bay.

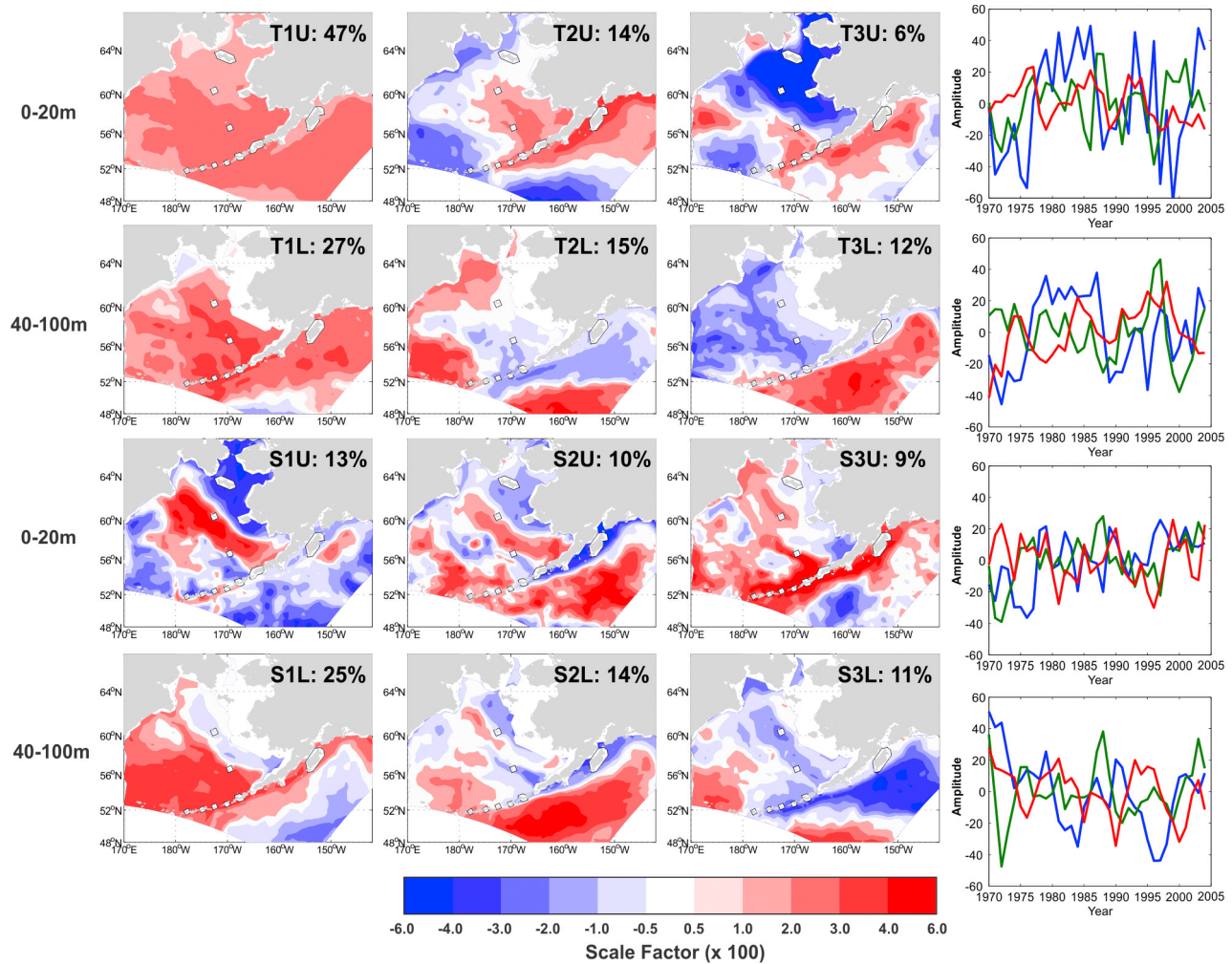


Figure 15. EOFs of the near-surface (0–20 m) and subsurface (40–100 m) temperature (first and second rows) and salinity (third and fourth rows) fields. Percentages describe the fraction of the total variance explained by each pattern. Also shown are the principal component amplitudes associated with the first (blue lines), second (green lines), and third (red lines) EOFs. EOF magnitudes are shown by the (nonlinear) color bar and are scaled by a factor of 10^2 .

[55] Modes T1L and T2L (the 40–100 m layer) resemble the spatial and temporal structure of their corresponding upper layer modes and are correlated with the PDO (T1L, $r = 0.69$) and NPGO (T2L, $r = -0.63$), respectively. While

T1L and T2L are more strongly correlated with these indices than T1U and T2U, they have a weaker correlation with ice extent ($r = -0.56$).

Table 5. Summary of Results of Correlations Between the Principal Components and Various Environmental Time Series^a

Index	T1U	T2U	T3U	S1U	S2U	S3U	T1L	T2L	T3L	S1L	S2L	S3L
PDO	0.59	0.21	0.10	0.22	0.30	-0.65	0.69	0.17	0.27	-0.55	0.27	0.40
NPGO	-0.36	0.47	-0.09	-0.18	0.51	0.39	-0.04	-0.63	-0.16	0.22	0.40	-0.57
AO	-0.31	-0.10	0.02	0.10	-0.13	0.27	-0.47	-0.19	0.04	0.07	-0.19	-0.28
PNA	0.15	0.54	0.05	0.02	0.37	-0.31	0.47	-0.14	0.21	-0.30	0.22	0.22
NP	-0.36	-0.25	-0.06	0.02	-0.24	0.57	-0.49	-0.05	-0.24	0.31	-0.23	-0.34
IIA	-0.67	-0.16	0.59	-0.79	-0.23	0.20	-0.56	-0.06	0.10	0.23	-0.20	-0.29
WDA	0.44	0.08	-0.38	0.52	0.13	0.06	0.44	0.11	-0.22	-0.03	0.20	0.09
GAK1 0–20 m T	0.25	0.23	-0.26	0.27	0.12	-0.33	0.36	0.01	0.16	-0.43	0.04	0.16
GAK1 0–20 m S	-0.22	-0.03	0.13	-0.16	0.12	0.27	-0.16	0.02	-0.04	0.23	0.02	-0.17
GAK1 200–250 m T	0.40	0.62	-0.07	0.24	0.70	-0.33	0.63	-0.36	0.28	-0.46	0.52	0.04
GAK1 200–250 m S	0.08	-0.12	-0.06	0.20	-0.03	0.23	-0.12	-0.29	-0.01	0.10	-0.19	-0.29
FWD	-0.07	0.56	0.22	-0.12	0.59	-0.12	0.24	-0.43	0.15	-0.07	0.43	-0.14

^aBoldface indicates relations that are significant at the 95% level. Three-character alphanumeric abbreviations distinguish temperature (T) and salinity (S) principal components 1–3 over upper (U, 0–20 m) and lower (L, 40–100 m) depth layers.

[56] Although the model has shortcomings in capturing the observed salinities, model salinity fields are internally consistent since these conform to the model dynamics. Hence, the modeled salinity variations, such as those presented in Figure 14 and discussed below, reflect physical processes that may bear on ecologically important processes.

[57] The first three upper layer salinity EOFs (Figure 15) represent a much smaller fraction of the total salinity variance than the corresponding temperature modes. For the 0–20 m layer, EOF S1U (13%) shows that the northeastern Bering shelf salinities are strongly out of phase with southwestern shelf salinities. This mode is correlated with the IIA ($r = -0.79$) and the WDA ($r = 0.52$) indices. The correlations suggest that the mode structure reflects salinization owing to ice formation processes in the northeast combined with ice melt in the southwest [Pease, 1980] and/or the winter cross-shelf transport of fresh coastal waters per Danielson *et al.* [2011]. Mode S2U (10%) is a weak out-of-phase relation between the middle shelf of the Bering Sea and the GOA shelf and in fact the pattern, when restricted to both shelves alone resembles the correlation structure in Figure 14. S2U is correlated to near-bottom temperatures at GAK1 ($r = 0.70$), GOA runoff ($r = 0.59$) and the PNA ($r = 0.37$). Higher GOA runoff is related to an eastward shift of the Aleutian Low (increase in the along-shore sea level pressure gradient) because it increases the precipitation rates over southeast Alaska [Weingartner *et al.*, 2005] and likely leads to less cooling of deep GOA coastal temperatures owing to enhanced stratification [Janout *et al.*, 2010]. This same atmospheric pattern forces enhanced ice growth (and salinization) over the northern Bering Sea shelf [Overland and Pease, 1982], so the model results appear to conform to our notion of regional thermohaline dynamics. EOF S3U is in phase along the GOA shelf and shelfbreak and along the Aleutian Islands and over the outer Bering shelf; the out of phase centers are in Bristol Bay and the western GOA basin. It is negatively correlated with the PDO ($r = -0.65$) and positively correlated with the NP index ($r = 0.57$). The continuity of the EOF patterns S2U and S3U from the GOA shelf across the Aleutians hints at an advective connection between the two regions, a connection that can be driven by the dependence of Unimak pass transport upon wind-forced sea level fluctuations [Schumacher *et al.*, 1982] and the distance of the Alaskan Stream axis from the passes [Favorite, 1974; Stabenho *et al.*, 2005].

[58] In the deeper layer, EOF S1L (25%) accounts for the largest percentage of salinity variability in any mode and is negatively correlated with the PDO ($r = -0.55$). The GOA shelf and Bering basin are in phase with each other for S1L and out of phase with the outer Bering shelf and GOA basin. Hence, salinities tend to increase (decrease) over the central GOA and outer Bering shelf, and decrease (increase) over the Bering Sea basin. This is consistent with the wind anomalies associated with the PDO [Mantua *et al.*, 1997]. In the positive phase of the PDO, cyclonic wind stress curl strengthens over the central GOA basin (carrying excess precipitation to the south-central coastal GOA) and weakens over the Bering basin. In addition southerly wind anomalies develop over the eastern Bering shelf and slope, possibly resulting in stronger upwelling along the shelfbreak. Mode S2L is primarily a GOA shelf/basin mode with the GOA shelf signal perhaps extending for a few degrees of latitude along the Bering Sea

shelfbreak. EOF S3L is correlated with the NPGO ($r = -0.57$) and is out of phase between the central GOA and the western Bering basin. The pattern implies that when the NPGO is in its positive phase, salinity anomalies increase within the GOA gyre, presumably owing to enhanced upwelling in the gyre center. The S3L pattern is similar to the structure of EOFs T2U and T2L, which are also both correlated to the NPGO.

[59] Note that the various EOFs do not necessarily correspond to recognized Large Marine Ecosystem boundaries [Sherman, 1991; Francis and Hare, 1994] or the Bering Sea shelf's biophysical domains [Coachman, 1986]. For example, T2U closely links the eastern Bering Sea with the GOA shelf, S2L depicts an apparent connection between the GOA shelf and the eastern Bering continental slope, and S3L shows that the central GOA basin and the outer Bering shelf fluctuate in concert.

5.4. Biological Covariates

[60] With these patterns of physical variability in hand we now ask if there are simple statistically significant relationships (Table 6) between these modes and indices that measure variability within the Bering Sea ecosystem (Table 3). Although pinpointing mechanistic links between EOF and biological covariates is outside the focus of this paper, we briefly describe a few relations.

[61] Significant correlations (at the 95% level) are found with species that span many trophic levels. Spring bloom, chlorophyll, primary productivity and condition indices for pollock, yellowfin sole and pacific cod are short ($N = 7$ or 8) but all are significantly correlated to one or more principal components. Longer ($N = 23$ – 35) fish and shellfish time series that correlate to the principal components include walleye pollock (T1U), pacific herring (T3U), rock sole (T3U, S1U, S2U, S2L), capelin (S1U), yellowfin sole (S3U, S1L), snow crab (T2U, T1L) and a number of multispecies composite indices (T2U, S3U, T2L, T3L, S2L). For those time series with at least 15 effective degrees of freedom, the EOFs account for up to 36% of the observed variability.

[62] Snow crabs are a commercially important epibenthic species whose distribution has fluctuated with temperature changes [Zheng *et al.*, 2001] although repopulation of southern regions following warm periods can be difficult [Orensanz *et al.*, 2004]. Mode T1L (strongest correlation to the PDO) captures 35% of the variance ($N = 25$) within the snow crab spawner-recruitment index. Fluctuation of mode T3U (apparently related to the winter position of the Aleutian Low and the sea ice extent) is positively correlated with the Togiak pacific herring stocks ($r = 0.62$, $N = 27$) and negatively correlated with rock sole ($r = -0.52$, $N = 30$). The strongly negative pattern of T3U over the Bering Shelf resembles the mean winter's end ice extent and so these correlations may reflect population dynamics tied to the annual preconditioning set by the winter ice extent or the wind and current regime that helps define the ice system. Should a changing climate tend to favor one phase of mode T3U over the other, the relation indicates that either the Togiak herring or the rock sole stock would benefit and the other would suffer.

[63] The above relations show that the NEP5 model output can be a useful tool for targeted retrospective studies of biological responses to environmental change. The NEP5 model is also being integrated forward in time on the basis of

Table 6. Temporal Correlations Between Ecosystem Indicator Time Series and the Principal Components^a

Index	<i>r</i>	$ r_c $	N	EDOF
<i>T1U</i>				
Average annual condition index (summer) for walleye Pollock	0.87	0.75	7	5
Average annual condition index (summer) for Pacific cod	0.86	0.82	8	4
<i>T2U</i>				
Total net primary production (May–November) over southeastern Bering Sea shelf	-0.85	0.75	7	5
Residuals from a spawner-recruitment relationship for snow crab	0.44	0.42	25	20
Temperature-adjusted depth distribution of 39 species in bottom trawl survey	-0.47	0.46	23	17
<i>T3U</i>				
Total mature biomass of Togiak stock of Pacific herring based on stock assessment	0.62	0.58	27	10
Female spawning stock biomass of rock sole based on stock assessment results	-0.52	0.48	30	15
<i>S1U</i>				
Index of capelin abundance from summer bottom trawl survey	-0.60	0.44	23	18
Female spawning stock biomass of rock sole based on stock assessment	0.46	0.44	30	18
Estimated abundance index for common murrens at St. Paul Island	-0.41	0.38	29	25
Productivity index for red-legged kittiwakes at St. Paul Island	-0.43	0.40	25	23
Productivity index for red-legged kittiwakes at St. George Island	-0.39	0.37	29	27
Phenology of red-legged kittiwakes at St. Paul Island	0.41	0.40	24	22
<i>S2U</i>				
Estimated onset of spring bloom over inner shelf	-0.87	0.75	7	5
Recruitment of age 4 rock sole by year class	0.54	0.48	33	15
Counts of common murrens at index sites on St. George Island	-0.63	0.58	12	10
Phenology of red-legged kittiwakes at St. Paul Island	-0.48	0.41	24	21
Phenology of common murrens at St. George Island	-0.42	0.40	27	23
<i>S3U</i>				
Estimated onset of spring bloom near mooring M2	0.78	0.77	7	5
Female spawning stock biomass of yellowfin sole based on stock assessment results	-0.35	0.35	35	30
Average annual condition index (summer) for yellowfin sole	-0.83	0.77	8	5
Temperature-adjusted depth distribution of 39 species in bottom trawl survey	-0.45	0.44	23	18
<i>T1L</i>				
Estimated spring stratification date on middle shelf near mooring M2	-0.39	0.37	35	27
Estimated onset of spring bloom over inner shelf	-0.81	0.75	7	5
Recruitment of juvenile snow crab by approximate year class (25–50 mm, age ~5)	0.56	0.47	29	16
Residuals from a spawner-recruitment relationship for snow crab	0.59	0.53	25	12
Average annual condition index (summer) for Pacific cod	0.72	0.71	8	6
Walleye pollock size-at-age anomalies during summer for the first age that is adequately sampled by summer trawl survey	0.82	0.79	7	4
Phenology of black-legged kittiwakes at St. George Island	0.40	0.37	28	26
Phenology of common murrens at St. George Island	-0.48	0.44	27	19
<i>T2L</i>				
Combined groundfish stock standardized index of recruitment across 11 stocks	-0.55	0.41	35	21
Temperature-adjusted depth distribution of 39 species from bottom trawl survey	0.49	0.46	23	17
Counts of common murrens at index sites on St. George Island	0.62	0.59	12	9
<i>T3L</i>				
Average downward shift in depth distribution of 39 species in bottom trawl survey	0.46	0.41	23	21
Productivity index for black-legged kittiwakes at St. Paul Island	-0.51	0.42	25	20
Productivity index for common murrens at St. Paul Island	-0.61	0.59	18	9
<i>S1L</i>				
Total yellowfin sole biomass based on 2007 stock assessment (age 2+)	-0.64	0.62	35	9
Female spawning stock biomass of yellowfin sole based on stock assessment results	-0.65	0.62	35	8
Productivity index for black-legged kittiwakes at St. Paul Island	0.55	0.43	25	19
Productivity index for common murrens at St. George Island	0.53	0.46	20	17
First principal component of seabird productivity time series	0.48	0.43	25	19
CS St. Paul Island thick-billed murre	-0.65	0.49	20	15
Phenology of common murrens at St. Paul Island	0.57	0.49	28	15

Table 6. (continued)

Index	r	$ r_c $	N	EDOF
<i>S2L</i>				
Estimated onset of spring bloom over inner shelf	-0.95	0.91	7	3
Recruitment of age 1 walleye pollock by year class	-0.38	0.36	35	28
Recruitment of age 4 rock sole by year class	0.45	0.39	33	24
Gadid recruitment anomaly: average of normalized pollock and cod recruitment series	-0.43	0.40	27	23
First principal component of fish recruitment series	-0.45	0.43	26	19
Residuals from a spawner-recruitment relationship for walleye pollock	-0.47	0.40	35	23
Average annual condition index (summer) for yellowfin sole	0.87	0.79	8	4
Average downward shift in depth distribution of 39 species in bottom trawl survey	-0.47	0.41	23	21
Phenology of red-legged kittiwakes at St. Paul Island	-0.46	0.41	24	21
Phenology of thick-billed murrelets at St. Paul Island	-0.60	0.46	28	17
Phenology of black-legged kittiwakes at St. George Island	0.50	0.40	28	23
<i>S3L</i>				
Estimated onset of spring bloom over southeast Bering shelf based on SeaWiFS	-0.95	0.92	7	2

^aAll relations are significant at the 95% level. Abbreviations are as follows: r , correlation coefficient; r_c , critical value; N, number of years; ED OF, effective degrees of freedom. Three-character alphanumeric principal component abbreviations distinguish temperature (T) and salinity (S) EOF modes 1–3 over upper (U, 0–20 m) and lower (L, 40–100 m) depth layers.

Intergovernmental Panel on Climate Change (IPCC) future climate scenarios. Examining stability of the modes and possible trends in their principal components within the forecast simulations together with the hindcast biological correlations may provide researchers the ability to diagnose potential ecosystem impacts of climate change, to the extent that the correlated relationships reflect stationary processes. Identifying mechanistic links between the biophysical covariates should remain a topic of high priority in future Bering Sea research.

6. Concluding Remarks

[64] Our analyses show that a number of lower and upper tropic level population indices are related to the physical variability predicted by the NEP5 results. The model results allow us to complement the limited set of physical observations and examine spatial and temporal patterns of variability. In aggregate, this approach has provided additional insights on ecosystem variations, or at least suggested future directions for examining this variability.

[65] The application of a 35 year ocean-ice hindcast to the Bering Sea shelf region provides some insights to the variability of the sea ice and thermohaline conditions on the Bering Sea shelf. Model strengths include the ability to reproduce 85% of the annually integrated ice variability and up to 50% of the monthly temperature variability; weaknesses include the low skill in reproducing monthly salinity anomalies and somewhat overly energetic circulation fields. Although the model provides some useful proxy time series in regions that lack observational data, it does not capture all of the in situ variability and improving the hindcast skill remains a high priority for the future.

[66] Model improvements that are currently being implemented will provide additional utility and should strengthen several of the comparisons made above. These modifications include: the incorporation of a coastal discharge field that contains both monthly and interannual variability [Dai et al., 2009], the relaxation of the northern boundary condition so that the Bering Strait fluxes can more realistically respond to the instantaneous wind field and a spatially varying light

attenuation coefficient. Our initial investigations suggest that accounting for water opacity improves the bottom temperature high bias seen in NEP5. Presumably these improvements will lead to a better mechanistic understanding of this shelf ecosystem, its variability, and perhaps its future trajectory. In the meantime, this work provides a baseline set of model evaluations that will help guide future improvements, applications and analyses.

[67] **Acknowledgments.** The authors thank the numerous researchers whose data have made the model/data evaluations presented herein possible. In particular, Lisa Eisner and the BASIS program have kindly provided CTD survey data. Peggy Sullivan tracked down many historical mooring positions. Zygmunt Kowalik graciously provided his compilation of historical amplitude and current tidal harmonic parameters and helped implement and evaluate the tidal forcing. We thank Franz Mueter for the use of his ecosystem indicator time series, helpful discussions, and statistical guidance. We thank Paul Budgett and one anonymous reviewer for thoughtful, constructive reviews that strengthened the manuscript. Mooring M2 data are provided by and supported through the NOAA EcoFOCI program. The Arctic Region Supercomputing Center at UAF, the National Center for Atmospheric Research, and the Texas Advanced Computing Center provided computational resources. This is publication 3769 from Pacific Marine Environmental Laboratory, North Pacific Research Board publication 312, and BEST-BSIERP Bering Sea Project publication 28. This work was supported by the Department of Interior Bureau of Ocean Energy Management, award M07PC13368, and the National Science Foundation, awards ARC-0732771, ARC-0732431, and ARC-0957985.

References

- Aagaard, K., T. J. Weingartner, S. L. Danielson, R. A. Woodgate, G. C. Johnson, and T. E. Whitledge (2006), Some controls on flow and salinity in Bering Strait, *Geophys. Res. Lett.*, *33*, L19602, doi:10.1029/2006GL026612.
- Andrews, A. G., R. A. Heintz, and E. V. Farley (2011), Age 1 walleye pollock in the eastern Bering Sea: Distribution, abundance, diet, and energy density, paper presented at Alaska Marine Science Symposium, Alaska Bering Sea Crabbers, Anchorage, Alaska.
- Arctic Climate Impact Assessment (ACIA) (2005), *Arctic Climate Impact Assessment*, 1042 pp., Cambridge Univ. Press, Cambridge, U. K.
- Benson, A. J. and A. W. Trites (2002), Ecological effects of regime shifts in the Bering Sea and eastern North Pacific Ocean, *Fish Fish.*, *3*, 95–113.
- Bering Ecosystem Study and Bering Sea Integrated Ecosystem Research Project (BEST-BSIERP) (2010), Program summary, North Pac. Res. Board, Anchorage, Alaska. [Available at http://doc.nprb.org/web/BSIERP/zzWebsite/proj_mgmt/01.10_bsag_web.pdf].

- Bograd, S. J., R. Mendelssohn, F. B. Schwing, and A. J. Miller (2005), Spatial heterogeneity of sea surface temperature trends in the Gulf of Alaska, *Atmos. Ocean*, *43*, 241–247, doi:10.3137/ao.430304.
- Boyer, T. P., et al. (2009), *World Ocean Database, NOAA Atlas NESDIS 66*, edited by S. Levitus, 216 pp., U.S. Gov. Print. Off., Washington, D. C.
- Brasseur, P. P. (1991), A variational inverse method for the reconstruction of general circulation fields in the northern Bering Sea, *J. Geophys. Res.*, *96*, 4891–4907, doi:10.1029/90JC02387.
- British Oceanographic Data Centre (2003), GEBCO digital atlas: Centenary edition of the IOC/IHO general bathymetric chart of the oceans [CD-ROM], Liverpool, U. K.
- Brodeur, R. D., H. Sugisaki, and G. L. Hunt Jr. (2002), Increases in jellyfish biomass in the Bering Sea: Implications for the ecosystem, *Mar. Ecol. Prog. Ser.*, *233*, 89–103, doi:10.3354/meps233089.
- Brodeur, R. D., M. B. Decker, L. Ciannelli, J. E. Purcell, N. A. Bond, P. J. Stabeno, E. Acuna, and G. L. Hunt Jr. (2008), Rise and fall of jellyfish in the eastern Bering Sea in relation to climate regime shifts, *Prog. Oceanogr.*, *77*, 103–111, doi:10.1016/j.pocean.2008.03.017.
- Budgell, W. P. (2005), Numerical simulation of ice-ocean variability in the Barents Sea region: Towards dynamical downscaling, *Ocean Dyn.*, *55*, 370–387, doi:10.1007/s10236-005-0008-3.
- Byrd, G. V., J. C. Williams, Y. B. Artukhin, and P. S. Vyatkin (1997), Trends in populations of red-legged Kittiwake *Rissa brevirostris*, a Bering Sea endemic, *Bird Conserv. Int.*, *7*, 167–180, doi:10.1017/S0959270900001489.
- Carton, J. A., and B. S. Giese (2008), A reanalysis of ocean climate using simple ocean data assimilation (SODA), *Mon. Weather Rev.*, *136*, 2999–3017, doi:10.1175/2007MWR1978.1.
- Cavalieri, D., C. Parkinson, P. Gloersen, and H. J. Zwally (1996), Sea Ice Concentrations from Nimbus-7 SMMR and DMSP SSM/I-SSMIS Passive Microwave Data, Natl. Snow and Ice Data Cent., Boulder, Colo. [Updated yearly.]
- Clarke, A. J., and D. S. Battisti (1981), The effect of continental shelves on tides, *Deep Sea Res.*, *28*, 665–682, doi:10.1016/0198-0149(81)90128-X.
- Clement, J. L., L. W. Cooper, and J. M. Grebmeier (2004), Late winter water column and sea-ice conditions in the northern Bering Sea, *J. Geophys. Res.*, *109*, C03022, doi:10.1029/2003JC002047.
- Clement, J. L., W. Maslowski, L. W. Cooper, J. M. Grebmeier, and W. Walczowski (2005), Ocean circulation and exchanges through the northern Bering Sea: 1979–2001, *Deep Sea Res., Part II*, *52*, 3509–3540, doi:10.1016/j.dsr2.2005.09.010.
- Clement Kinney, J., W. Maslowski, and S. Okkonen (2009), On the processes controlling shelf-basin exchange and outer shelf dynamics in the Bering Sea, *Deep Sea Res., Part II*, *56*, 1351–1362, doi:10.1016/j.dsr2.2008.10.023.
- Coachman, L. K. (1982), Flow convergence over a broad, flat continental shelf, *Cont. Shelf Res.*, *1*, 1–14.
- Coachman, L. K. (1986), Circulation, water masses, and fluxes on the southeastern Bering Sea shelf, *Cont. Shelf Res.*, *5*, 23–108, doi:10.1016/0278-4343(86)90011-7.
- Coachman, L. K., K. Aagaard, and R. B. Tripp (1975), *Bering Strait: The Regional Physical Oceanography*, 172 pp., Univ. of Wash. Press, Seattle.
- Comiso, J., D. J. Cavalieri, C. L. Parkinson, and P. Gloersen (1997), Passive microwave algorithms for sea ice concentration: A comparison of two techniques, *Remote Sens. Environ.*, *60*, 357–384, doi:10.1016/S0034-4257(96)00220-9.
- Coyle, K. O., A. I. Pinchuk, L. B. Eisner, and J. M. Napp (2008), Zooplankton species composition, abundance and biomass on the eastern Bering Sea shelf during summer: The potential role of water column stability and nutrients in structuring the zooplankton community, *Deep Sea Res., Part II*, *55*, 1775–1791, doi:10.1016/j.dsr2.2008.04.029.
- Curchitser, E. N., D. B. Haidvogel, A. J. Hermann, E. L. Dobbins, T. M. Powell, and A. Kaplan (2005), Multi-scale modeling of the North Pacific Ocean: Assessment and analysis of simulated basin-scale variability (1996–2003), *J. Geophys. Res.*, *110*, C11021, doi:10.1029/2005JC002902.
- Curchitser, E. N., K. Hedstrom, S. Danielson, and T. J. Weingartner (2010), Modeling of circulation in the North Aleutian Basin, *OCS Study BOEMRE 2010-028*, Bur. of Ocean Manage., U.S. Dep. of the Inter., Washington, D. C. [Available at http://alaska.boemre.gov/reports/2010rpts/2010_028.pdf.]
- Curry, J. A., J. E. Schramm, and E. E. Ebert (1995), On the ice albedo climate feedback mechanism, *J. Clim.*, *8*, 240–247, doi:10.1175/1520-0442(1995)008<0240:SIACFM>2.0.CO;2.
- Dai, A., T. Qian, K. E. Trenberth, and J. D. Milliman (2009), Changes in continental freshwater discharge from 1948–2004, *J. Climate*, *22*, 2773–2791.
- Danielson, S., and Z. Kowalik (2005), Tidal currents in the St. Lawrence Island region, *J. Geophys. Res.*, *110*, C10004, doi:10.1029/2004JC002463.
- Danielson, S., K. Aagaard, T. Weingartner, S. Martin, P. Winsor, G. Gawarkiewicz, and D. Quadfasel (2006), The St. Lawrence polynya and the Bering shelf circulation: New observations that test the models, *J. Geophys. Res.*, *111*, C09023, doi:10.1029/2005JC003268.
- Danielson, S., L. Eisner, T. Weingartner, and K. Aagaard (2011), Thermal and haline variability over the central Bering Sea shelf: Seasonal and inter-annual perspectives, *Cont. Shelf Res.*, *31*, 539–554, doi:10.1016/j.csr.2010.12.010.
- Defant, A. (1960), *Physical Oceanography*, vol. 2, 598 pp., Elsevier, New York.
- Di Lorenzo, E., et al. (2008), North Pacific Gyre Oscillation links ocean climate and ecosystem change, *Geophys. Res. Lett.*, *35*, L08607, doi:10.1029/2007GL032838.
- Dobbins, E. L., A. J. Hermann, P. J. Stabeno, N. A. Bond, and R. C. Steed (2009), Modeled transport of freshwater from a line-source in the coastal Gulf of Alaska, *Deep Sea Res., Part II*, *56*, 2409–2426, doi:10.1016/j.dsr2.2009.02.004.
- Favorite, F. (1974), Flow into the Bering Sea through Aleutian Island passes, in *Oceanography of the Bering Sea With Emphasis on Renewable Resources*, edited by D. W. Hood and E. J. Kelley, pp. 59–98, Inst. of Mar. Sci., Univ. of Alaska, Fairbanks.
- Fay, F. H. (1982), Ecology and biology of the Pacific walrus, *Odobenus rosmarus divergens Illiger*, *North Am. Fauna* *74*, 279 pp., U.S. Fish. and Wildlife Serv., Washington, D. C.
- Fiechter, J., A. M. Moore, C. A. Edwards, K. W. Bruland, E. Di Lorenzo, C. V. W. Lewis, T. M. Powell, E. N. Curchitser, and K. Hedstrom (2009), Modeling iron limitation of primary production in the coastal Gulf of Alaska, *Deep Sea Res., Part II*, *56*, 2503–2519, doi:10.1016/j.dsr2.2009.02.010.
- Foreman, M. G. G., W. R. Crawford, J. Y. Cherniawsky, R. F. Henry, and M. R. Tarbotton (2000), A high-resolution assimilating tidal model for the northeast Pacific Ocean, *J. Geophys. Res.*, *105*, 28,629–28,651, doi:10.1029/1999JC000122.
- Foreman, M. G. G., P. F. Cummins, J. Y. Cherniawsky, and P. Stabeno (2006), Tidal energy in the Bering Sea, *J. Mar. Res.*, *64*, 797–818, doi:10.1357/00224006779698341.
- Francis, R. C., and S. R. Hare (1994), Decadal-scale regime shifts in the large marine ecosystems of the northeast Pacific: A case for historical science, *Fish. Oceanogr.*, *3*, 279–291, doi:10.1111/j.1365-2419.1994.tb00105.x.
- Gibson, M. A., and S. B. Schullinger (1998), *Answer From the Ice Edge: The Consequences of Climate Change on Life in the Bering and Chukchi Seas*, Arctic Network, Greenpeace, Washington, D. C.
- Gill, A. E. (1982), *Atmosphere–Ocean Dynamics*, 662 pp., Academic, San Diego, Calif.
- Greisman, P. (1985), Western Gulf of Alaska tides and circulation, 112 pp., Natl. Oceanic and Atmos. Admin., Anchorage, Alaska.
- Haidvogel, D. B., and A. Beckman (1999), *Numerical Ocean Circulation Modeling*, vol. 2, *Ser. Environ. Sci. Manage.*, 318 pp., Imperial Coll. Press, London.
- Haney, R. L. (1991), On the pressure gradient force over steep topography in sigma coordinate ocean models, *J. Phys. Oceanogr.*, *21*, 610–619, doi:10.1175/1520-0485(1991)021<0610:OTPGFO>2.0.CO;2.
- Harrison, N. M., G. L. Hunt Jr., and R. T. Cooney (1990), Front affecting the distribution of seabirds in the northern Bering Sea, *Polar Res.*, *8*, 29–31, doi:10.1111/j.1751-8369.1990.tb00372.x.
- Heintz, R. A., and J. J. Vollenweider (2010), Influence of size on the sources of energy consumed by overwintering walleye pollock (*Theragra chalcogramma*), *J. Exp. Mar. Biol. Ecol.*, *393*, 43–50, doi:10.1016/j.jembe.2010.06.030.
- Hermann, A. J., P. J. Stabeno, D. B. Haidvogel, and D. L. Musgrave (2002), A regional tidal/subtidal circulation model of the southeastern Bering Sea: Development, sensitivity analyses and hindcasting, *Deep Sea Res., Part II*, *49*, 5945–5967, doi:10.1016/S0967-0645(02)00328-4.
- Hermann, A. J., E. N. Curchitser, D. B. Haidvogel, and E. L. Dobbins (2009a), A comparison of remote versus local influence of El Niño on the coastal circulation of the northeast Pacific, *Deep Sea Res., Part II*, *56*, 2427–2443, doi:10.1016/j.dsr2.2009.02.005.
- Hermann, A. J., S. Hinckley, E. L. Dobbins, D. B. Haidvogel, N. A. Bond, C. Mordy, N. Kachel, and P. J. Stabeno (2009b), Quantifying cross-shelf and vertical nutrient flux in the Gulf of Alaska with a spatially nested, coupled biophysical model, *Deep Sea Res., Part II*, *56*, 2474–2486, doi:10.1016/j.dsr2.2009.02.008.
- Hinckley, S., K. O. Coyle, G. Gibson, A. J. Hermann, and E. L. Dobbins (2009), A biophysical NPZ model with iron for the Gulf of Alaska: Reproducing the differences between an oceanic HNLC ecosystem and

- a classical northern temperate shelf ecosystem, *Deep Sea Res., Part II*, 56, 2520–2536, doi:10.1016/j.dsr.2009.03.003.
- Hu, H., and J. Wang (2010), Modeling effects of tidal and wave mixing on circulation and thermohaline structures in the Bering Sea: Process studies, *J. Geophys. Res.*, 115, C01006, doi:10.1029/2008JC005175.
- Hunke, E. C. (2001), Viscous-plastic sea ice dynamics with the EVP model: Linearization issues, *J. Comput. Phys.*, 170, 18–38, doi:10.1006/jcph.2001.6710.
- Hunke, E. C., and J. K. Dukowicz (1997), An elastic-viscous-plastic model for sea ice dynamics, *J. Phys. Oceanogr.*, 27, 1849–1867, doi:10.1175/1520-0485(1997)027<1849:AEVPMF>2.0.CO;2.
- Hunt, G. L., Jr., P. J. Stabeno, G. Walters, E. Sinclair, R. D. Brodeur, J. M. Napp, and N. A. Bond (2002), Climate change and control of the southeastern Bering Sea pelagic ecosystem, *Deep Sea Res., Part II*, 49, 5821–5853, doi:10.1016/S0967-0645(02)00321-1.
- Isaji, T., and M. L. Spaulding (1987), A numerical model of the 3/2 and K 1 tide in the northwestern Gulf of Alaska, *J. Phys. Oceanogr.*, 17, 698–704, doi:10.1175/1520-0485(1987)017<0698:ANMOTM>2.0.CO;2.
- Janout, M. A., T. J. Weingartner, T. C. Royer, and S. L. Danielson (2010), On the nature of winter cooling and the recent temperature shift on the northern Gulf of Alaska shelf, *J. Geophys. Res.*, 115, C05023, doi:10.1029/2009JC005774.
- Johnson, W., and Z. Kowalik (1986), Modeling of storm surges in the Bering Sea and Norton Sound, *J. Geophys. Res.*, 91, 5119–5128, doi:10.1029/JC091iC04p05119.
- Kachel, N. B., G. L. Hunt Jr., S. A. Salo, J. D. Schumacher, P. J. Stabeno, and T. E. Whitledge (2002), Characteristics and variability of the inner front of the southeastern Bering Sea, *Deep Sea Res., Part II*, 49, 5889–5909, doi:10.1016/S0967-0645(02)00324-7.
- Kantha, L. H., and G. L. Mellor (1989), A two-dimensional couple ice-ocean model of the Bering Sea marginal ice zone, *J. Geophys. Res.*, 94, 10,921–10,935, doi:10.1029/JC094iC08p10921.
- Kokubun, N., A. Takahashi, M. Ito, K. Matsumoto, A. S. Kitaysky, and Y. Watanuki (2010), Annual variation in the foraging behaviour of thick-billed murres in relation to upper-ocean thermal structure around St. George Island, Bering Sea, *Aquat. Biol.*, 8, 289–298, doi:10.3354/ab00243.
- Kowalik, Z. (1999), Bering sea tides, in *Dynamics of the Bering Sea: A Summary of Physical, Chemical, and Biological Characteristics, and a Synopsis of Research on the Bering Sea, Rep. AK-SG-99-03*, edited by T. R. Loughlin and K. Ohtani, pp. 93–127, North Pac. Mar. Sci. Org., Univ. of Alaska, Fairbanks.
- Kowalik, Z., and P. Stabeno (1999), Trapped motion around the Pribilof Islands in the Bering Sea, *J. Geophys. Res.*, 104, 25,667–25,684, doi:10.1029/1999JC900209.
- Lanksbury, J. A., J. T. Duffy-Anderson, K. L. Mier, M. S. Busby, and P. J. Stabeno (2007), Distribution and transport patterns of northern rock sole, *Lepidopsetta polyxystra*, larvae in the southeastern Bering Sea, *Prog. Oceanogr.*, 72, 39–62, doi:10.1016/j.pocan.2006.09.001.
- Large, W. G., and S. G. Yeager (2009), The global climatology of an interannually varying air-sea flux data set, *Clim. Dyn.*, 33, 341–364, doi:10.1007/s00382-008-0441-3.
- Large, W. G., J. C. McWilliams, and S. C. Doney (1994), Oceanic vertical mixing: A review and a model with a nonlocal boundary layer parameterization, *Rev. Geophys.*, 32, 363–403, doi:10.1029/94RG01872.
- Lovvorn, J. R., S. E. Richman, J. M. Grebmeier, and L. W. Cooper (2003), Diet and body condition of spectacled eiders wintering in pack ice of the Bering Sea, *Polar Biol.*, 26, 259–267, doi:10.1007/s00300-003-0477-0.
- Mantua, N., S. Hare, Y. Zhang, J. Wallace, and R. Francis (1997), A Pacific interdecadal climate oscillation with impacts on salmon production, *Bull. Am. Meteorol. Soc.*, 78, 1069–1079, doi:10.1175/1520-0477(1997)078<1069:APICOW>2.0.CO;2.
- Marchesiello, P., J. C. McWilliams, and A. Shchepetkin (2001), Open boundary conditions for long-term integration of regional oceanic models, *Ocean Modell.*, 3, 1–20.
- Mellor, G. L., and L. Kantha (1989), An ice-ocean coupled model, *J. Geophys. Res.*, 94, 10,937–10,954, doi:10.1029/JC094iC08p10937.
- Minobe, S. (1999), Resonance in bidecadal and pentadecadal climate oscillations over the North Pacific: Role in climate regime shifts, *Geophys. Res. Lett.*, 26, 855–858, doi:10.1029/1999GL900119.
- Mizobata, K., J. Wang, and S. Saitoh (2006), Eddy-induced cross-slope exchange maintaining summer high productivity of the Bering Sea shelf break, *J. Geophys. Res.*, 111, C10017, doi:10.1029/2005JC003335.
- Mofjeld, H. O. (1984), Recent observations of tides and tidal currents from the northeastern Bering Sea shelf, *Tech. Memo. ERL PMEL-57*, 36 pp., Natl. Oceanic and Atmos. Admin., Silver Spring, Md.
- Mofjeld, H. O. (1986), Observed tides on the northeastern Bering Sea shelf, *J. Geophys. Res.*, 91, 2593–2606, doi:10.1029/JC091iC02p02593.
- Mofjeld, H. O., J. D. Schumacher, and D. J. Pashinski (1984), Theoretical and observed profiles of tidal currents at two sites on the southeastern Bering sea shelf, *Tech. Memo. ERL PMEL-62*, 60 pp., Natl. Oceanic and Atmos. Admin., Silver Spring, Md.
- Mooers, C. N. K. (1973), A technique for the cross spectrum analysis of pairs of complex-valued time series, with emphasis on properties of polarized components and rotational invariants, *Deep Sea Res.*, 20, 1129–1141.
- Muench, R. D., and J. D. Schumacher (1980), Physical oceanographic and meteorological conditions in the northwest Gulf of Alaska, *Tech. Memo. ERL PMEL-22*, 147 pp., Natl. Oceanic and Atmos. Admin., Silver Spring, Md.
- Muench, R. D., J. D. Schumacher, and S. A. Salo (1988), Winter currents and hydrographic conditions on the northern central Bering Sea Shelf, *J. Geophys. Res.*, 93, 516–526, doi:10.1029/JC093iC01p00516.
- Mueter, F. J., and M. A. Litzow (2008), Sea ice retreat alters the biogeography of the Bering Sea continental shelf, *Ecol. Appl.*, 18, 309–320, doi:10.1890/07-0564.1.
- Napp, J. M., C. T. Baier, K. O. Coyle, R. D. Brodeur, N. Shiga, and K. Mier (2002), Interannual and decadal variability in zooplankton communities of the southeastern Bering Sea, *Deep Sea Res., Part II*, 49, 5991–6008, doi:10.1016/S0967-0645(02)00330-2.
- Niebauer, H. J. (1998), Variability in the Bering Sea ice cover as affected by a regime shift in the North Pacific in the period 1947–1996, *J. Geophys. Res.*, 103, 27,717–27,737, doi:10.1029/98JC02499.
- Nihoul, J. C. J., P. Adam, P. Brasseur, E. Deleersnijder, S. Djenidi, and J. Haus (1993), Three-dimensional general circulation model of the northern Bering Sea's summer ecohydrodynamics, *Cont. Shelf Res.*, 13, 509–542, doi:10.1016/0278-4343(93)90093-D.
- North, G. R., T. L. Bell, R. F. Cahalan, and F. J. Moeng (1982), Sampling errors in the estimation of empirical orthogonal functions, *Mon. Weather Rev.*, 110, 699–706, doi:10.1175/1520-0493(1982)110<0699:SEITEO>2.0.CO;2.
- North Pacific Fishery Management Council (NPFMC) (2005), *Fishery Management Plan for Groundfish of the Bering Sea and Aleutian Islands Management Area*, Anchorage, Alaska.
- Oey, L.-Y., T. Ezer, C. Hu, and F. Muller-Karger (2007), Baroclinic tidal flows and inundation processes in Cook Inlet, Alaska: Numerical modeling and satellite observations, *Ocean Dyn.*, 57, 205–221, doi:10.1007/s10236-007-0103-8.
- Orensanz, J., B. Ernst, D. Armstrong, P. Stabeno, and P. Livingston (2004), Contraction of the geographic range of distribution of snow crab (*Chionoecetes opilio*) in the eastern Bering Sea: An environmental ratchet?, *CalCOFI Rep.*, 45, 65–79.
- Orr, V. (2011), As ice melts, new opportunities, challenges arise for Alaska's northern communities, *Alaska Bus. Mon.*, pp. 46–55, March.
- Overland, J. E., and C. H. Pease (1982), Cyclone climatology of the Bering Sea and its relation to sea ice extent, *Mon. Weather Rev.*, 110, 5–13, doi:10.1175/1520-0493(1982)110<0005:CCOTBS>2.0.CO;2.
- Overland, J. E., and A. T. Roach (1987), Northward flow in the Bering and Chukchi seas, *J. Geophys. Res.*, 92, 7097–7105, doi:10.1029/JC092iC07p07097.
- Overland, J. E., M. C. Spillane, H. Y. Hurlbert, and A. J. Wallcraft (1994), A numerical study of the circulation of the Bering Sea basin and exchange with the North Pacific Ocean, *J. Phys. Oceanogr.*, 24, 736–758, doi:10.1175/1520-0485(1994)024<0736:ANSOTC>2.0.CO;2.
- Overland, J. E., J. M. Adams, and N. A. Bond (1999), Decadal variability of the Aleutian low and its relation to high latitude circulation, *J. Clim.*, 12, 1542–1548, doi:10.1175/1520-0442(1999)012<1542:DVOTAL>2.0.CO;2.
- Pawlowski, R., B. Beardsley, and S. Lentz (2002), Classical tidal harmonic analysis including error estimates in MATLAB using T_TIDE, *Comput. Geosci.*, 28, 929–937, doi:10.1016/S0098-3004(02)00013-4.
- Pearson, C. A., H. O. Mofjeld, and R. B. Tripp (1981), Tides of the eastern Bering Sea shelf, in *The Eastern Bering Sea Shelf: Oceanography and Resources*, edited by D. W. Hood and J. A. Calder, pp. 111–130, U.S. Dep. of Comm., Washington, D. C.
- Pease, C. H. (1980), Eastern Bering Sea ice processes, *Mon. Weather Rev.*, 108, 2015–2023, doi:10.1175/1520-0493(1980)108<2015:EBSSIP>2.0.CO;2.
- Pease, C. H., and J. E. Overland (1989), An atmospherically driven sea ice drift model for the Bering Sea, *Ann. Glaciol.*, 5, 111–114.
- Petersen, M. R., W. W. Larned, and D. C. Douglas (1999), At-sea distribution of spectacled eiders: A 120-year-old mystery resolved, *Auk*, 116, 1009–1020.
- Prandle, D. (1982), The vertical structure of tidal current, *Geophys. Astrophys. Fluid Dyn.*, 22, 29–49, doi:10.1080/03091928208221735.

- Pritchard, R. S., A. C. Mueller, D. J. Hanzlick, and Y. S. Yang (1990), Forecasting Bering Sea ice edge behavior, *J. Geophys. Res.*, *95*, 775–788, doi:10.1029/JC095iC01p00775.
- Pyper, B. J., and R. M. Peterman (1998), Comparison of methods to account for autocorrelation in correlation analysis of fish data, *Can. J. Fish. Aquat. Sci.*, *55*, 2127–2140, doi:10.1139/f98-104.
- Roach, A. T., K. Aagaard, C. H. Pease, S. A. Salo, T. Weingartner, V. Pavlov, and M. Kulakov (1995), Direct measurements of transport and water properties through Bering Strait, *J. Geophys. Res.*, *100*, 18,443–18,457, doi:10.1029/95JC01673.
- Rodionov, S. N., N. A. Bond, and J. E. Overland (2007), The Aleutian Low, storm tracks, and winter climate variability in the Bering Sea, *Deep Sea Res., Part II*, *54*, 2560–2577, doi:10.1016/j.dsr2.2007.08.002.
- Røed, L. P., and J. Debernard (2004), Description of an integrated flux and sea-ice model suitable for coupling to an ocean atmosphere model, *Rep. 4*, 51 pp., Norw. Meteorol. Inst., Oslo.
- Royer, T. C. (1982), Coastal fresh water discharge in the northeast Pacific, *J. Geophys. Res.*, *87*, 2017–2021, doi:10.1029/JC087iC03p02017.
- Schumacher, J. D., and T. H. Kinder (1983), Low-frequency current regimes over the Bering Sea shelf, *J. Phys. Oceanogr.*, *13*, 607–623, doi:10.1175/1520-0485(1983)013<0607:LFCROT>2.0.CO;2.
- Schumacher, J. D., and R. K. Reed (1992), Characteristics of currents over the continental slope of the eastern Bering Sea, *J. Geophys. Res.*, *97*, 9423–9433, doi:10.1029/92JC00512.
- Schumacher, J. D., and P. J. Stabeno (1998), Continental shelf of the Bering Sea, in *The Sea*, vol. 11, *The Global Coastal Ocean: Regional Studies and Synthesis*, edited by A. R. Robinson and K. H. Brink, pp. 789–822, John Wiley, New York.
- Schumacher, J. D., C. A. Pearson, and J. E. Overland (1982), On exchange of water between the Gulf of Alaska and the Bering Sea through Unimak Pass, *J. Geophys. Res.*, *87*, 5785–5795, doi:10.1029/JC087iC08p05785.
- Schumacher, J. D., K. Aagaard, C. Pease, and R. Tripp (1983), Effects of a shelf polynya on flow and water properties in the northern Bering Sea, *J. Geophys. Res.*, *88*, 2723–2732, doi:10.1029/JC088iC05p02723.
- Schumacher, J. D., N. A. Bond, R. D. Brodeur, P. A. Livingston, J. M. Napp, and P. J. Stabeno (2003), Climate change in the southeastern Bering Sea and some consequences for biota, in *Large Marine Ecosystems of the World*, edited by G. Hempel and K. Sherman, pp. 17–40, Elsevier, Amsterdam.
- Sherman, K. (1991), The large marine ecosystem concept: Research and management strategy for living marine resources, *Ecol. Appl.*, *1*, 349–360, doi:10.2307/1941896.
- Spaulding, M., T. Isaji, D. Mendelsohn, and A. C. Turner (1987), Numerical simulation of wind-driven flow through the Bering Strait, *J. Phys. Oceanogr.*, *17*, 1799–1816, doi:10.1175/1520-0485(1987)017<1799:NSOWDF>2.0.CO;2.
- Stabeno, P. J., and R. K. Reed (1994), Circulation in the Bering Sea basin by satellite tracked drifters, *J. Phys. Oceanogr.*, *24*, 848–854, doi:10.1175/1520-0485(1994)024<848:CITBSB>2.0.CO;2.
- Stabeno, P. J., and P. Van Meurs (1999), Evidence of episodic on-shelf flow in the southeastern Bering Sea, *J. Geophys. Res.*, *104*, 29,715–29,720, doi:10.1029/1999JC900242.
- Stabeno, P. J., J. D. Schumacher, and K. Ohtani (1999), The physical oceanography of the Bering Sea, in *Dynamics of the Bering Sea: A Summary of Physical, Chemical, and Biological Characteristics, and a Synopsis of Research on the Bering Sea, Rep. AK-SG-99-03*, edited by T. R. Loughlin and K. Ohtani, pp. 1–28, North Pac. Mar. Sci. Org., Univ. of Alaska, Fairbanks.
- Stabeno, P. J., R. K. Reed, and J. M. Napp (2002a), Transport through Unimak Pass, Alaska, *Deep Sea Res., Part II*, *49*, 5919–5930, doi:10.1016/S0967-0645(02)00326-0.
- Stabeno, P. J., N. B. Kachel, M. Sullivan, and T. E. Whitledge (2002b), Variability of physical and chemical characteristics along the 70-m isobath of the southeast Bering Sea, *Deep Sea Res., Part II*, *49*, 5931–5943, doi:10.1016/S0967-0645(02)00327-2.
- Stabeno, P. J., D. G. Kachel, N. B. Kachel, and M. E. Sullivan (2005), Observations from moorings in the Aleutian Passes: Temperature, salinity and transport, *Fish. Oceanogr.*, *14*, 39–54, doi:10.1111/j.1365-2419.2005.00362.x.
- Stabeno, P. J., J. Napp, C. Mordy, and T. Whitledge (2010), Factors influencing physical structure and lower trophic levels of the eastern Bering Sea shelf in 2005: Sea ice, tides and winds, *Prog. Oceanogr.*, *85*, 180–196, doi:10.1016/j.pocean.2010.02.010.
- Steele, M., G. L. Mellor, and M. G. McPhee (1989), Role of the molecular sublayer in the melting or freezing of sea ice, *J. Phys. Oceanogr.*, *19*, 139–147, doi:10.1175/1520-0485(1989)019<0139:ROTMSI>2.0.CO;2.
- Steele, M., R. Morley, and W. Ermold (2001), PHC: A global ocean hydrography with a high-quality arctic ocean, *J. Clim.*, *14*, 2079–2087, doi:10.1175/1520-0442(2001)014<2079:PAGOHW>2.0.CO;2.
- Stephens, C., S. Levitus, J. Antonov, and T. P. Boyer (2001), On the Pacific Ocean regime shift, *Geophys. Res. Lett.*, *28*, 3721–3724, doi:10.1029/2000GL012813.
- Stockwell, D. A., T. E. Whitledge, S. I. Zeeman, K. O. Coyle, J. M. Napp, R. D. Brodeur, A. I. Pinchuk, and G. L. Hunt (2001), Anomalous conditions in the southeastern Bering Sea, 1997: Nutrients, phytoplankton and zooplankton, *Fish. Oceanogr.*, *10*, 99–116, doi:10.1046/j.1365-2419.2001.00158.x.
- Sugimoto, T., and K. Tadokoro (1997), Interannual–interdecadal variations in zooplankton biomass, chlorophyll concentration and physical environment in the subarctic Pacific and Bering Sea, *Fish. Oceanogr.*, *6*, 74–93, doi:10.1046/j.13652419.1997.00031.x.
- Takenouti, A. Y., and K. Ohtani (1974), Currents and water masses in the Bering Sea: A review of Japanese work, in *Oceanography of the Bering Sea With Emphasis on Renewable Resources*, edited by D. W. Hood and E. J. Kelley, pp. 39–57, Inst. of Mar. Sci., Univ. of Alaska, Fairbanks.
- Taylor, K. E. (2001), Summarizing multiple aspects of model performance in a single diagram, *J. Geophys. Res.*, *106*, 7183–7192, doi:10.1029/2000JD900719.
- Trenberth, K. E., and J. W. Hurrell (1994), Decadal atmosphere–ocean variations in the Pacific, *Clim. Dyn.*, *9*, 303–319, doi:10.1007/BF00204745.
- Trites, A. W., P. A. Livingston, M. C. Vasconcellos, S. Mackinson, A. M. Springer, and D. Pauly (1999), Ecosystem change and the decline of marine mammals in the eastern Bering Sea: Testing the ecosystem shift and commercial whaling hypotheses, *Res. Rep. 7*, 106 pp., Fish. Cent., Univ. of B. C., Vancouver, B. C., Canada.
- Wang, J., H. Hu, K. Mizobata, and S. Saitoh (2009), Seasonal variations of sea ice and ocean circulation in the Bering Sea: A model–data fusion study, *J. Geophys. Res.*, *114*, C02011, doi:10.1029/2008JC004727.
- Weingartner, T. J., S. L. Danielson, and T. C. Royer (2005), Freshwater variability and predictability in the Alaska Coastal Current, *Deep Sea Res., Part II*, *52*, 169–191, doi:10.1016/j.dsr2.2004.09.030.
- Wespestad, V. G., L. W. Fritz, W. J. Ingraham, and B. A. Megrey (2000), On relationships between cannibalism, climate variability, physical transport and recruitment success of Bering Sea walleye pollock (*Theragra chalcogramma*), *ICES J. Mar. Sci.*, *57*, 272–278, doi:10.1006/jmsc.2000.0640.
- Wessel, P., and W. H. F. Smith (1991), Free software helps map and display data, *Eos Trans. AGU*, *72*(41), 441, doi:10.1029/90EO00319.
- Willmott, C. J., S. G. Ackleson, R. E. Davis, J. J. Feddema, K. M. Klink, D. R. Legates, J. O'Donnell, and C. M. Rowe (1985), Statistics for the evaluation and comparison of models, *J. Geophys. Res.*, *90*, 8995–9005, doi:10.1029/JC090iC05p08995.
- Woodgate, R. A., K. Aagaard, and T. J. Weingartner (2005), Monthly temperature, salinity, and transport variability of the Bering Strait through flow, *Geophys. Res. Lett.*, *32*, L04601, doi:10.1029/2004GL021880.
- Zhang, J., and W.D. Hibler III (1991), On the role of ocean circulation in seasonal and interannual ice-edge variations in the Bering Sea, *Ann. Glaciol.*, *15*, 37–44.
- Zhang, J., R. Woodgate, and R. Moritz (2010), Sea ice response to atmospheric and oceanic forcing in the Bering Sea, *J. Phys. Oceanogr.*, *40*, 1729–1747, doi:10.1175/2010JPO4323.1.
- Zheng, J., G. H. Kruse, and D. R. Ackley (2001), Spatial distribution and recruitment patterns of snow crabs in the eastern Bering Sea, in *Spatial Processes and Management of Marine Populations, Rep. AK-SG-01-02*, edited by G. H. Kruse et al., pp. 233–255, Alaska Sea Grant Coll. Prog., Univ. of Alaska, Fairbanks.

E. Curchitser, Institute of Marine and Coastal Sciences, Rutgers, State University of New Jersey, New Brunswick, NJ 08901, USA.

S. Danielson and T. Weingartner, School of Fisheries and Ocean Science, Institute of Marine Science, University of Alaska Fairbanks, Rm. 114, O'Neill Building, Fairbanks, AK 99775-7220, USA. (seth@ims.uaf.edu)

K. Hedstrom, Arctic Region Supercomputing Center, University of Alaska Fairbanks, Fairbanks, AK 99775, USA.

P. Stabeno, Pacific Marine Environmental Laboratory, NOAA, 7600 Sand Point Way, Seattle, WA 98115-6349, USA.